STScI | SPACE TELESCOPE SCIENCE INSTITUTE

JWST TECHNICAL REPORT

Title: The Population of Cosmic Rays and Snowballs Detected in the JWST NIRISS Instrument	Doc #: JWST-STScI-008875, SM-12 Date: 21 November 2024 Rev: -
Authors: A.R. Martel, R. Cooper, & K. Volk Phone: 410-338-4888	Release Date: 4 December 2024

1 Abstract

The JWST NIRISS instrument is continuously subjected to the harsh radiation environment of L2, leading to a slow degradation of its optical and electronic components. To understand the impact of the cosmic rays (CRs) on its science performance, we have begun monitoring and trending the population of CRs and snowballs in long full-frame dark exposures collected at regular intervals in Cycles 1 and 2 as part of the calibration programs PID 1497 and 4473. We find that the fluxes of the CRs and snowballs correlate with the solar cycle, showing a decrease in the flux of CRs of about 35% from August 2022 to June 2024. The CR flux correlates with the fluxes of background particles detected by the GOES-18 satellite in geosynchronous orbit and the ACE satellite at L1. Some exposures show highly elevated CR fluxes that can be attributed to extreme solar events. Showers and clusters of CRs become more frequent as the solar activity increases. The dark current rate and bias level of the dark exposures also correlate with the flux of CRs on the detector. Some possible causes for this relationship are discussed.

2 Introduction

At the end of the 6-month commissioning campaign of the James Webb Space Telescope (JWST), the Near-Infrared Imager and Slitless Spectrograph (NIRISS) began its normal calibration and science operations (Doyon et al. 2023; Martel et al. 2023; Rigby et al. 2023). As part of the Cycle 1 and 2 calibration effort, the programs with ID (PID)1497 (PI: Martel) and PID 4473 (PI: Cooper) were implemented to monitor the health and behavior of the detector by collecting full-frame darks at regular intervals. Importantly, the darks also serve to update multiple types of reference files in the Calibration Reference Data System (CRDS) of the JWST science calibration pipeline (Bushouse et al. 2024). The primary reference files derived from the darks are the superbias, read noise, dark rate, and the bad pixel mask. The initial on-orbit detector properties and reference files were analyzed and created by Cooper et al. (2023) using the darks gathered during the commissioning campaign.

The dark exposures can also serve to monitor and trend the population of solar and Galactic CRs that impinge on the HgCdTe detector and electronics of NIRISS. At its halo orbit at L2, JWST is immersed in the relatively steady plasma from the solar wind and, at times, in the Earth's complex geomagnetic tail (Evans et al. 2003). The dominant components of this plasma are protons and electrons and a small proportion of alpha particles ($\approx 5\%$ of the number of protons). Solar flares and coronal mass ejections (CMEs) also represent another source of energetic particles. These sporadic and eruptive solar particle events (SPEs) are generally more frequent near the peak of the solar cycle, when the number of sunspots reaches a maximum, and typically last a few hours or days. Lastly, a steady flow of high-energy Galactic cosmic rays (GCRs) originating outside the heliosphere is another source of ionizing radiation at L2. They consist primarily of protons (90%), alpha particles (9%), and heavy nuclei (1%) and are believed to be accelerated in shocks produced when supernova ejecta expand into the interstellar medium (ISM) (Blasi 2013). The flux of GCRs is modulated and anti-correlated with the solar cycle due to the variability and dynamics of the magnetic field of the heliosphere (Potgieter 2013; Fu et al. 2021).

These three sources of ionizing radiation can have serious deleterious effects on the detector and on-board electronics of NIRISS. Single event upsets (SEUs) from GCRs and high-energy particles in the solar flares can interrupt the operation of electronic components. Long-term exposure can lead to a cumulative degradation of the semiconductor layers of the detector by "displacement damage", leading to permanent defects in the crystal lattice that can cause charge traps and possibly changes in the band gap. This likely explains the steady growth in the number of non-linear resistor capacitor (RC) pixels in the NIRISS detector since the on-orbit operations began. These new, unusable pixels must be regularly added to the bad pixel mask. The transmission and reflection properties of the coatings of optical components can also be adversely affected.

In the following, the population of CRs and snowballs observed in the long dark exposures of NIRISS in Cycles 1 and 2 are characterized. The NIRISS detector is a 2048×2048 HgCdTe device built by Teledyne Imaging Sensors and sensitive to wavelengths of $0.6\ \mu$m to $5\ \mu$m. The CRs are typically small (a few pixels), compact, and circular. Some can strike the detector at a large grazing incidence and produce extended, narrow trails that can span a large portion of the detector. Snowballs are significantly less numerous than CRs or trails. They are large (up to several hundreds of pixels in area), circular, and their high energies saturate their cores. Similar to CRs, snowballs are omnipresent in the space-based exposures of the HgCdTe detectors of the JWST instruments. They are most likely caused by high-energy space particles and have been detected in other space observatories such as HST WFC3/IR (Green & Olszewski 2020), Euclid, and WFIRST (now the Nancy Grace Roman Space Telescope) (Cillis et al. 2018). Snowballs were also observed in the ground calibration campaigns, likely originating from the radioactive decay of impurities in the detectors (McCullough 2009), early in the lifetime of the detectors. They are described in detail by Volk (2014) in the ground detector characterization campaign of NIRISS. We discuss the origin of the CRs and snowballs in more detail in this report.

3 Dark Exposures

Operationally, NIRISS collects dark exposures by crossing the short-wavelength F158M filter in the Pupil Wheel (PW) with the long-wavelength F430M filter in the Filter Wheel (FW). In Table A-1 (Appendix A), a journal of the PID 1497 and 4473 darks is presented. All the exposures consist of five integrations of 120 groups read out with the NISRAPID pattern. The exposure time is therefore 1.80 hours. The temperature setpoint of the Focal Plane Array (FPA) is 39.00 K and the variability of the FPA temperature is only ± 0.0001 K over intervals of a few hours (Martel et al. 2022). Telemetry extracted from the Work Offline Workspace (WOW) indicates that the temperature of the FPA decreases slightly (≈ 0.001 K), when each exposure begins and then slowly increases to about 0.0005 K below its starting value at the mid-point of the exposure. Conversely, the temperature of the Application Specific Integrated Circuit (ASIC) increases gradually as the exposure progresses and after 30 min, it stabilizes ≈ 0.06 K higher than its starting value. At the end of the exposure, the temperatures of the FPA and ASIC return to near their initial values. As Fig. 3-1 shows, the FPA and ASIC temperatures increased steadily by about 0.06% and 0.8%, respectively, over the ≈ 2 year period of data collection, until a small adjustment to the setting of the FGS/NIRISS trim heater was made on June 17, 2024. This activity slightly decreased the FPA and ASIC temperatures when the last two darks (4473:39 and 4473:40) were acquired. These small changes in the FPA and ASIC temperature have no significant impact on the behavior of the dark rates nor on the population of bad pixels, CR hits, and snowballs.

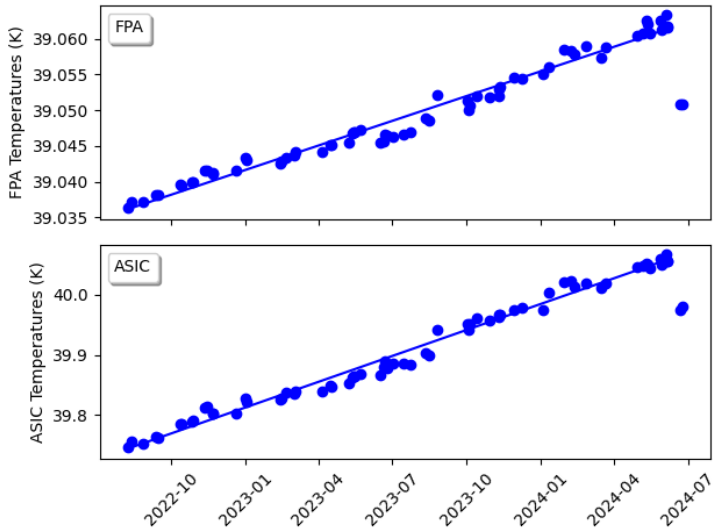

Figure 3-1. The temperatures of the FPA and ASIC are plotted over the period the darks were collected.

Two darks were excluded from the sample. For the dark exposure of 4473:9 (2023-09-15), the FPA temperature had reached 40.59 K because of a runaway thermal escalation following the load of SIDECAR Build 10.2 to the Observatory. The FPA was later reset and the temperatures returned to normal. In 4473:14 (2023-12-19), the dark exhibits count rates several percents greater than normal. The source of this glow is believed to be scattered moonshine (E. Bergeron; private communication; February 19, 2024). Some darks also show some very faint features in the bottom-left quadrant of the detector. These are 1497:11, 1497:31, 1497:33, 1497:38, and 4473:6. As discussed in Martel et al. (2023), these features can likely be attributed to persistence

as the NIRISS detector was idling on a field of bright astronomical sources in a preceding program, up to several hours earlier. The darks of 1497:41 and 4473:15 also exhibit a faint residual signal from previous exposures in the SUB64 and SUB128 corner subarrays and in the SUB80 subarray, respectively. The low signal in these regions doesn't affect our measurements of the CRs and snowballs, so these darks are retained in our sample.

4 Pipeline Processing

The Level1b exposures (*_uncal.fits) were downloaded from the Mikulski Archive for Space Telescopes (MAST) at the Space Telescope Science Institute (STScI) and processed with the JWST pipeline version 1.13.4 and the CRDS context jwst_1202.pmap to produce the Level2a slope images (*_rateints.fits and *_rate.fits; units of ADU/sec) as well as the intermediate ramp product (*_ramp.fits; in ADUs) (Bushouse et al. 2024). The data quality initialization, jump detection, linearity correction, reference pixel correction, ramp fitting, saturation checking, and superbias subtraction were all performed with the default reference files available at the time of the processing. The CRs and snowballs are identified as jumps in counts (or signal) (ADUs) between consecutive groups in the jump step, as described in Regan (2024). The parameter *after_jump_flag_time_1* in the jump step parameter reference file (jwst_niriss_pars-jumpstep_0075.asdf) is set to 90 sec by default in order to exclude the eight groups that immediately follow the group initially hit by a CR or snowball from the slope calculations. But since these eight groups are also flagged as ramp jumps in the GROUPDQ array (GROUPDQ = 4), the true number of CR hits in a ramp are significantly overcounted. Therefore, for the identification of the CR hits, this parameter is set to a value of 0 sec so that only the group where the CR hit first occurs is flagged as a jump. For the characterization of the slope of the segments preceding and following a CR hit, this parameter is set to the default value of 90 sec (Section 5.4).

The identification and measurements of the properties of the CRs and snowballs are made on the ramp exposures. Data models of the SCI and GROUPDQ extensions of each integration are created with the RampModel class in the jwst.datamodels package of the calibration pipeline. Pixels with GROUPDQ = 1 (DO_NOT_USE) in the 4-pixel-wide reference pixels and in the 1-pixel-wide border surrounding the imaging area are uniformly set to a null value. But in the imaging area, the GROUPDQ arrays have values of 0 (good pixels) or combinations of the three bit-wise flag values: 1 (DO_NOT_USE; bad pixels, predominantly single pixels), 2 (SATURATED), and 4 (JUMP_DET; applicable to CRs and snowballs). Pixels with a GROUPDQ value of 1 (or that include this value in their combinations) are replaced by the mean of their surrounding pixels in the imaging array. If the pixel has a GROUPDQ = 5, a CR hit atop a bad pixel, then the GROUPDQ of the repaired pixel is replaced by a value of 4. Otherwise, the GROUPDQ of the repaired pixel is set to 0. All the bad pixels in the final, corrected image array of each group have therefore been corrected by the mean of their surrounding pixels. The final GROUPDQ array of each group has values of 0, 2, or 4.

5 Classification of the CRs, Snowballs, and Trails

Clusters with three or more contiguous pixels with a JUMP_DET value in the GROUPDQ array of each group of a ramp are identified with the *fclusterdata* method of the hierarchical clustering package of *SciPy*. The measurements are made in all the groups of each of the five integrations of a ramp. The centroid, ellipticity, and position angle (PA) of the major axis of each cluster are calculated with their moments. After closely examining the morphology of the

clusters, we converged on three classification categories: CRs, snowballs, and CR trails. The ellipticity and PA of the small clusters ($N_{pix} \leq 10$) are unreliable so they are simply classified as CRs. Slightly larger clusters ($10 < N_{pix} \leq 15$) with relatively small ellipticities ($e \leq 0.3$) are also classified as CRs. The CRs have no saturated pixels. Large clusters ($N_{pix} > 15$) with a small ellipticity ($e \leq 0.3$) and at least two saturated pixels in their cores are labeled as snowballs. Large, elongated clusters ($N_{pix} > 10$ and $e > 0.3$) are classified as trails. Admittedly, these criteria are somewhat subjective but they prevent the large, thin trails of grazing CRs that traverse a large area of the detector from being included in the sample of the smaller and symmetric CRs.

In Figs 5-1 and 5-2, the distributions of the size of all the CRs and snowballs in the dark exposure of 1497:11 are shown. The majority of the CRs have a size of eight pixels or less. The snowballs show a wide range of sizes and the largest can reach almost 500 pixels. Representative examples of the SCI and GROUPDQ extensions of a CR, snowball, and trail are shown in Figs 5-3 to 5-5. These size distributions and morphologies are typical for all the dark exposures.

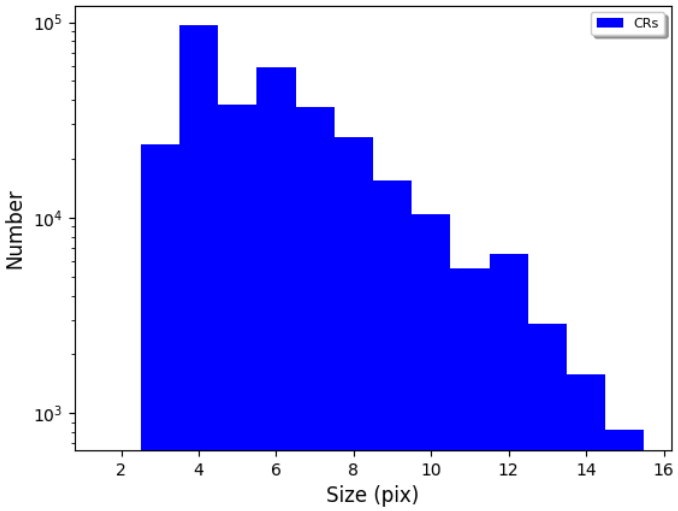

Figure 5-1. Distribution of the size of the CRs in the dark exposure of 1497:11.

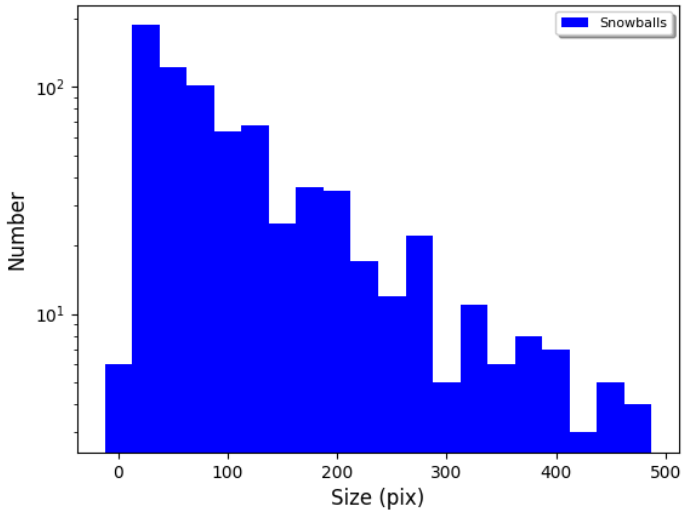

Figure 5-2. Distribution of the size of the snowballs in the dark exposure of 1497:11.

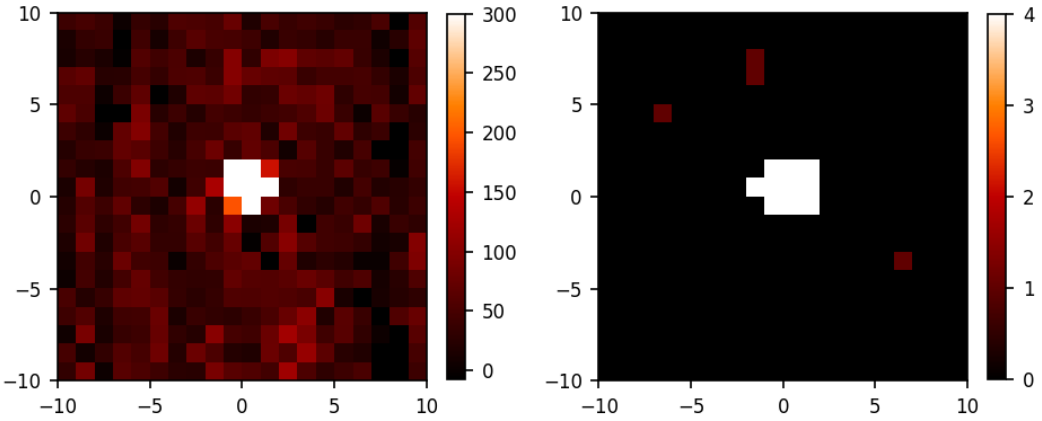

Figure 5-3. Left: A CR in the SCI extension of the first integration and fourth group of the dark of 1497:5. The size of the CR is 10 pix. Right: The corresponding GROUPDQ array in the same integration and group. The pixels of the CR have a value of JUMP_DET = 4.

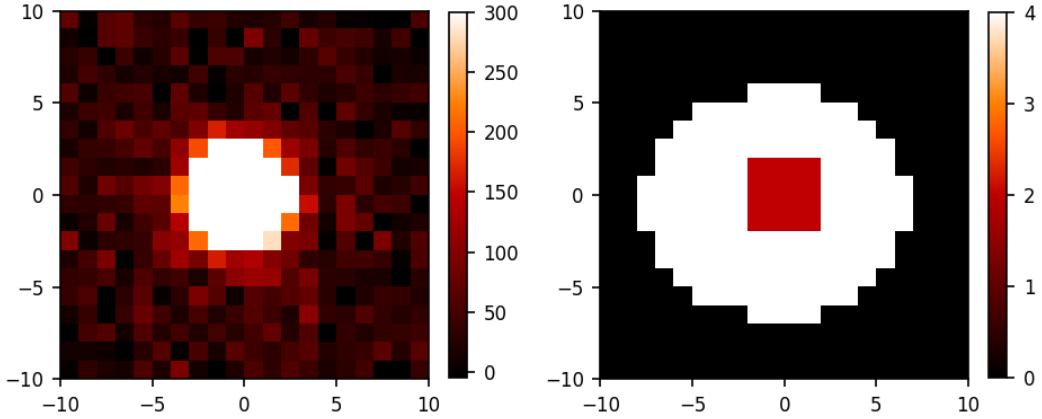

Figure 5-4. Left: A snowball in the SCI extension of the first integration and fourth group of the dark of 1497:5. The size of the snowball is 145 pix. Right: The corresponding GROUPDQ array in the same integration and group. The pixels of the snowballs have a value of SATURATED = 2 in the core and JUMP_DET = 4 outside.

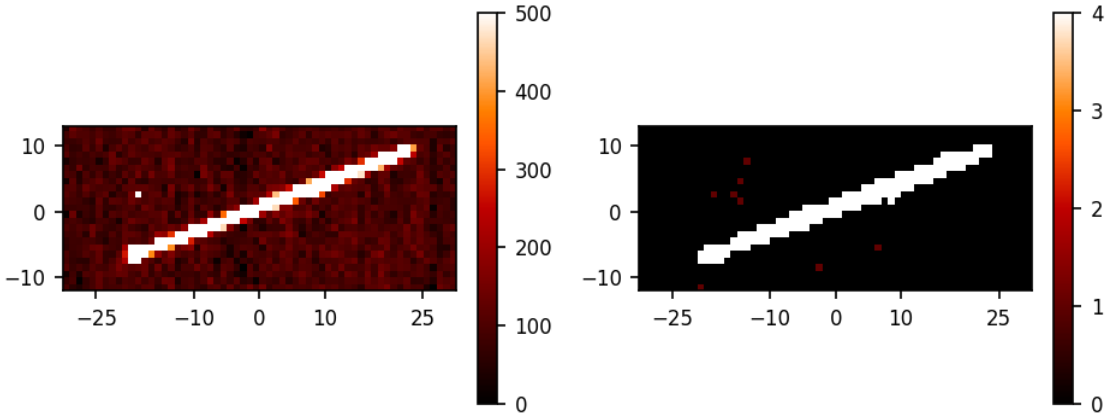

Figure 5-5. Left: A CR trail in the SCI extension of the first integration and third group of the dark of 1497:5. The size of the trail is 131 pix. Right: The corresponding GROUPDQ array in the same integration and group. The pixels of the trail have a value of JUMP_DET = 4.

The number of CR and snowball events are converted to flux units of number of CRs per thousand pixels per second ($N_{CRs}/10^3 - \text{pix}/\text{sec}$) and number of snowballs per million pixels per second ($N_{snow}/10^6 - \text{pix}/\text{sec}$) for consistency with the FITS header keywords PRIMECRS and EXTNCRS. To convert to these units, we assume the particles impact the imaging area of the detector (2040×2040 pix^2) and the frame time is TFRAME = 10.737 sec. The total signal of the CRs and trails are calculated by summing over the pixels of the identified cluster. Since the dark rate is small and does not produce a significant accumulation of signal between consecutive groups, the signal in the same pixels of the preceding group are treated as background and subtracted. Because of the heavy saturation of their cores, the snowballs are not included in the analysis of the signal. The signal is converted to e^- with the average NIRISS detector gain of $1.61\ e^-/\text{ADU}$.

6 Results

We report our results on the flux of CRs and snowballs, the randomness of the spatial distribution of the CRs, and the impact of the solar activity on the CRs, the dark count rate, and the bias level over the 2-year period of the PID 1497 and 4473 programs.

6.1 Flux of CRs, Snowballs, and Trails

In Fig. 6-1, the flux of CRs throughout Cycles 1 and 2 is shown. Since the data of each 2-hour dark appear compressed on such a long timescale, an enlargement is shown in Fig. 6-2 for the dark of 1497:29 (2023-03-02). In these figures, the flux of CRs in each group of the five integrations is represented with blue dots and their median with a red dot. The error bars on the median are simply three times the standard deviation. For reference, a value of $1.0 \times 10^{-2}\ \text{CRs}/10^3 - \text{pix}/\text{sec}$ represents 447 CRs in one group. Over the 2-year timespan of the darks, the overall flux decreases smoothly and appears to level off around January 2024. From August 2022 (1497:5) to June 2024 (4473:40), we observe a decrease of about 35% in the CR flux, $1.182 \times 10^{-2}\ \text{CRs}/10^3 - \text{pix}/\text{sec}$ (528 CRs per group) to $7.654 \times 10^{-3}\ \text{CRs}/10^3 - \text{pix}/\text{sec}$ (342 CRs per group).

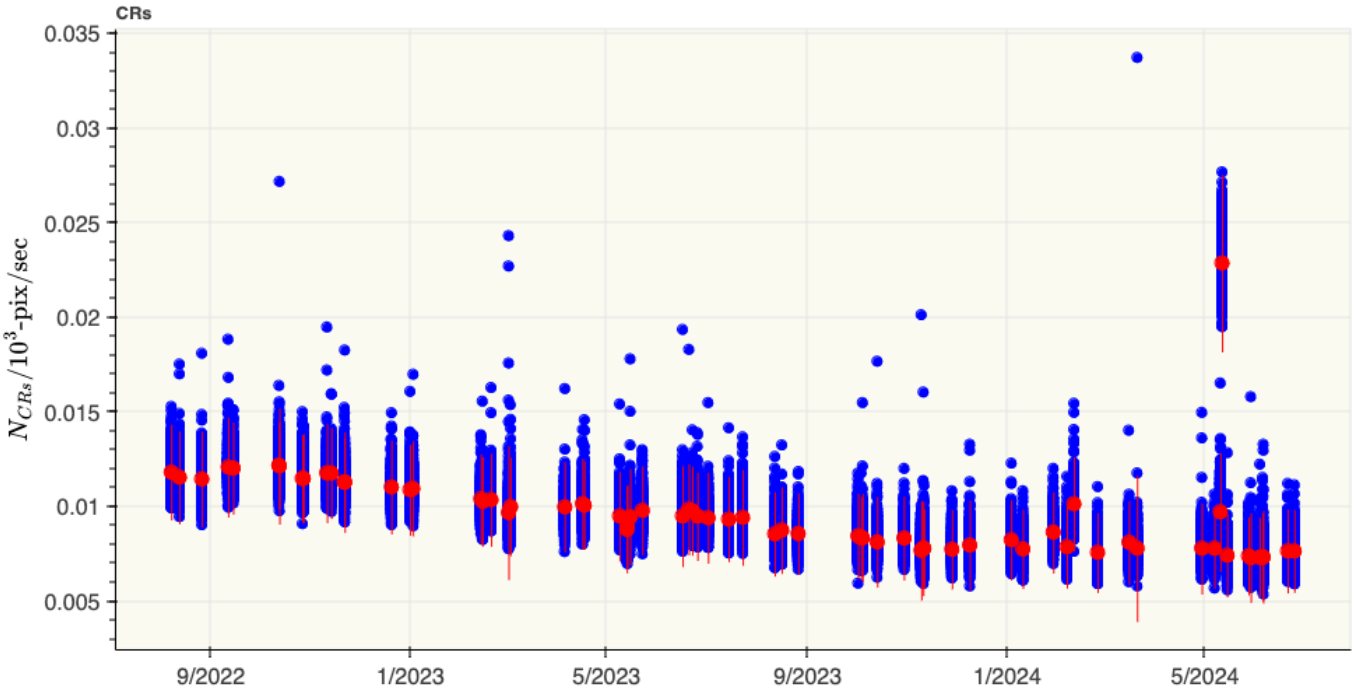

Figure 6-1. The flux of CRs in each dark exposure is plotted as blue dots. The median value is shown in red and the error bars are three times the standard deviation.

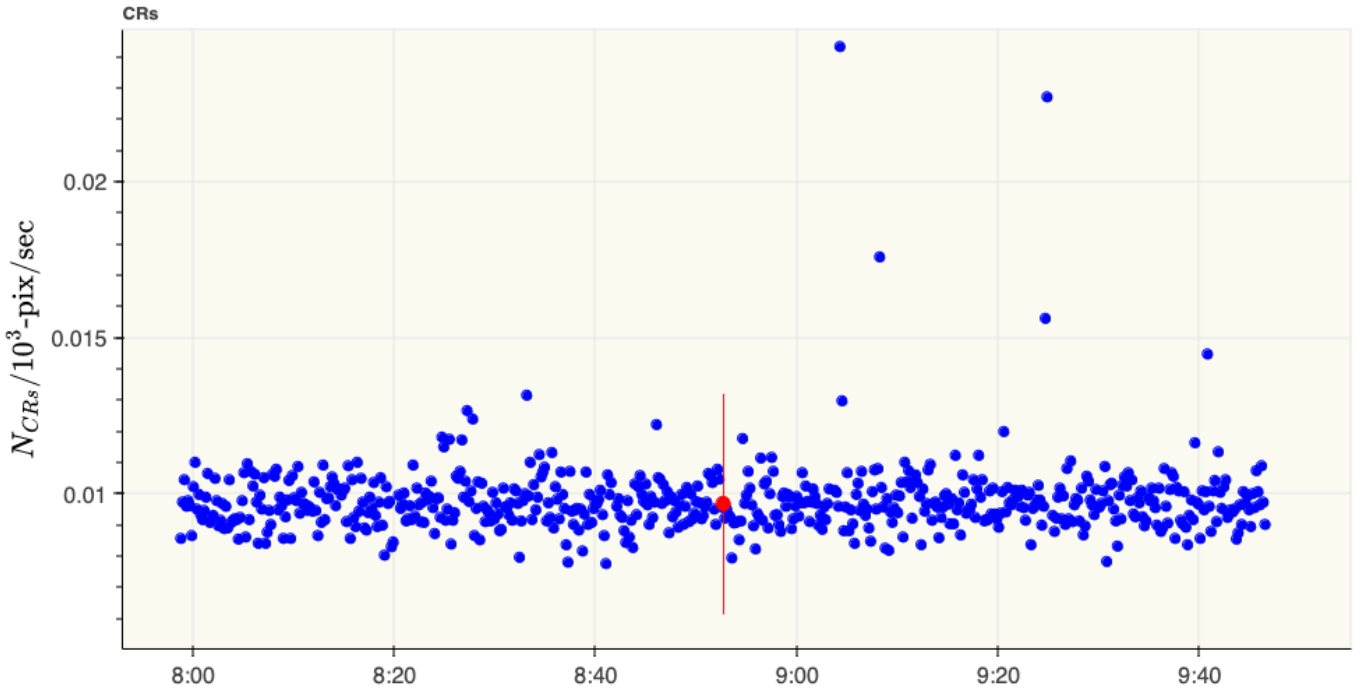

Figure 6-2. An enlargement of the dark of 1497:29 (2023-03-02) showing the flux of CRs in each group of the five integrations.

During a typical dark exposure, e.g., Fig. 6-2, the flux of the CRs in each group is constant except for a few groups that show a pronounced excess, up to a factor of ~4 greater than the median in the most extreme case, 4473:30 (2024-03-20). But three darks show unusually elevated fluxes in all their groups compared to the darks that immediately precede and follow them: 4473:25 (2024-02-11) and the two darks of 4473:31 (2024-05-10) and 4473:35 (2024-05-11) collected within one day of each other. As seen in Fig. 6-1, the flux of 4473:35 is the most significant outlier, with a median flux of 2.287×10^{-2} CRs/10^3 − pix /sec, about three times greater than that of the surrounding darks. Moreover, unlike a typical dark that shows a constant CR flux as the exposure progresses through its five integrations, the flux of these darks shows significant and unusual structure, as shown in Figs 6-3 to 6-5. For 4473:25, the flux increases steadily by about 6% from beginning to end. The CR flux of 4473:31 is relatively constant in the first half of the exposure and then rises by about 20% before decreasing to its original value. The flux of the dark of 4473:35 shows the most dramatic behavior, declining steeply by 20% throughout the exposure. We note that the CR flux of the dark of 4473:36 taken three days after 4473:35, although not unusually elevated, shows a weak positive slope of about 4%. In Section 6.3.2, we will show that the remarkable behavior of the CR flux of these darks is due to unusually intense SPEs.

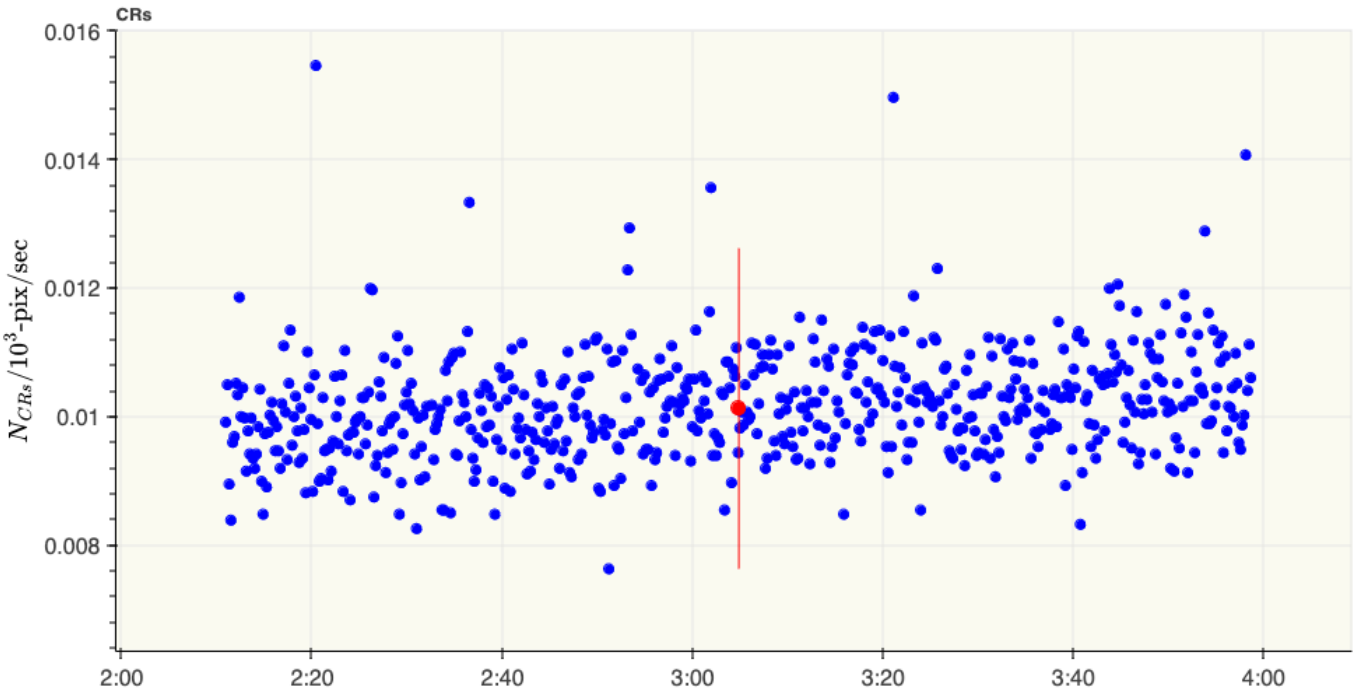

Figure 6-3. Same as Fig. 6-2 but for the dark of 4473:25 (2024-02-11).

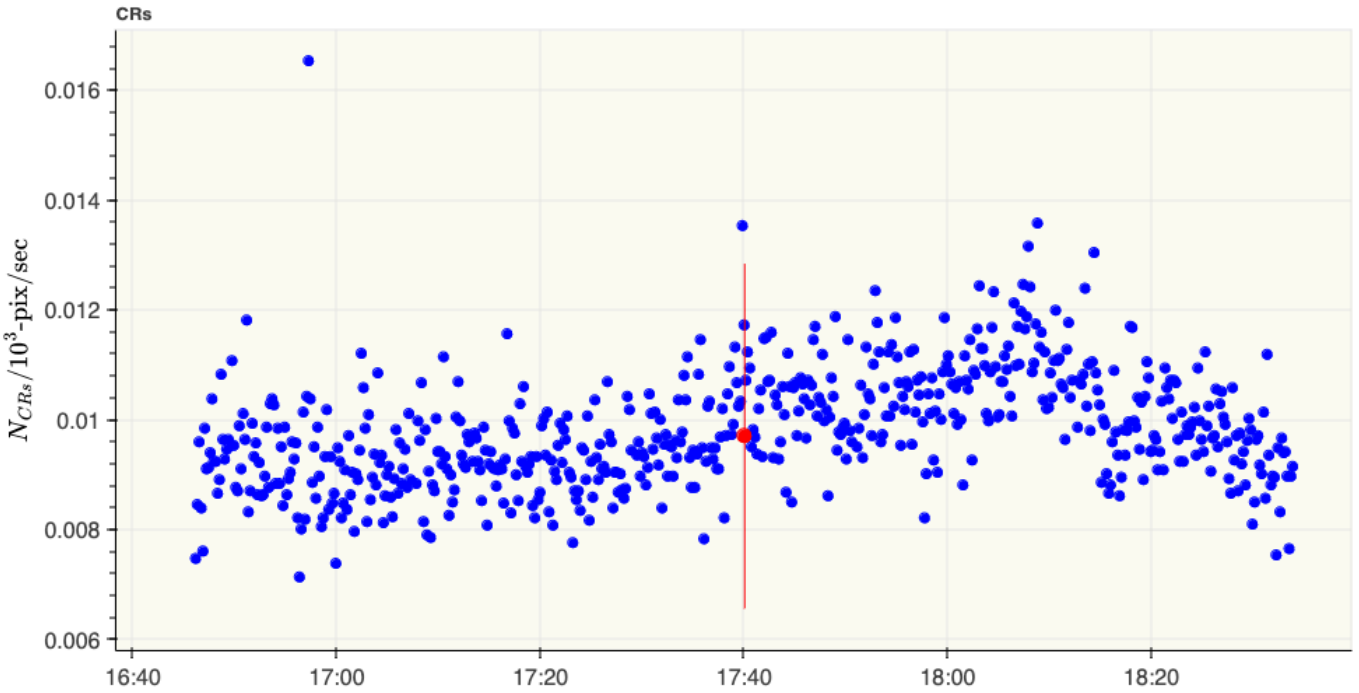

Figure 6-4. Same as Fig. 6-2 but for the dark of 4473:31 (2024-05-10).

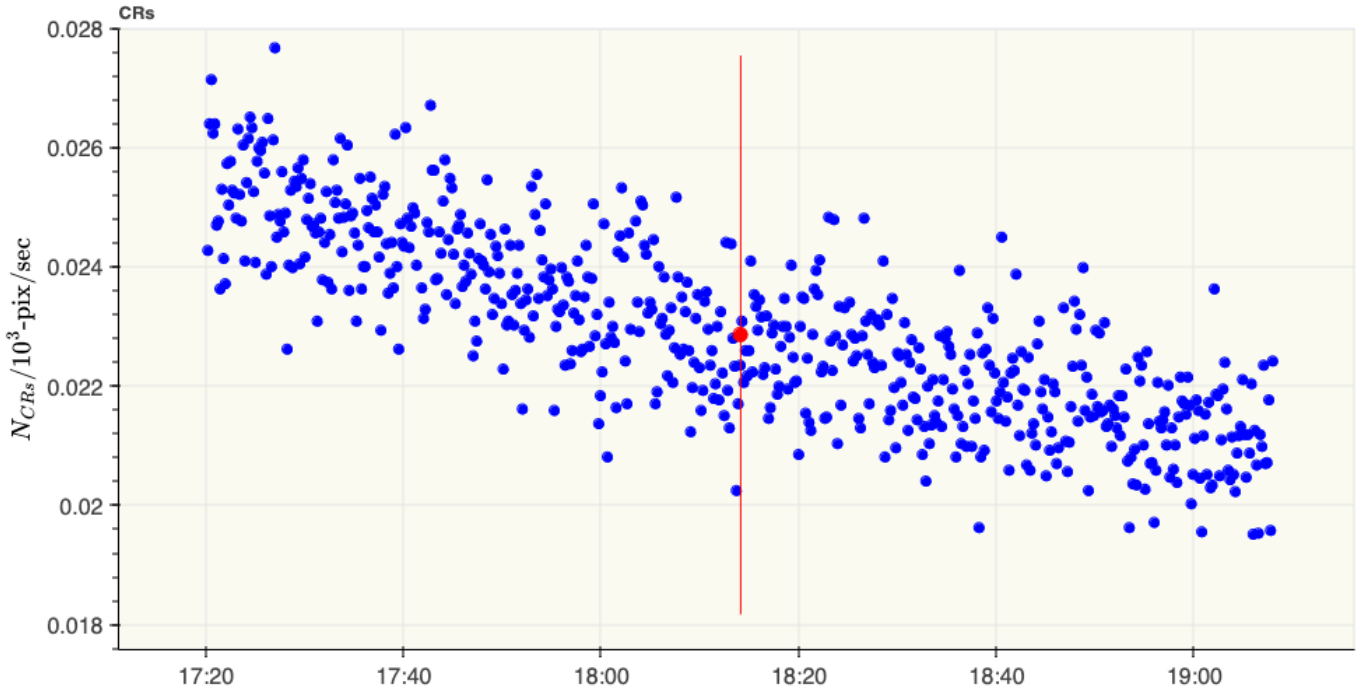

Figure 6-5. Same as Fig. 6-2 but for the dark of 4473:35 (2024-05-11).

In Fig. 6-6, the flux of the snowballs in the dark exposures is shown. Typically, the snowball flux varies from about 2.238×10^{-2} snowballs$/10^6 -$ pix /sec (one snowball per group) up to 0.246 snowballs$/10^6 -$ pix /sec (10 snowballs per group). Some groups do not possess any snowballs. As for its CR flux, the dark of 4473:35 shows an exceptionally large range of snowball fluxes, $2.238 \times 10^{-2} - 0.425$ snowballs$/10^6 -$ pix /sec (1 – 17 snowballs per group) and a median flux of 8.952×10^{-2} snowballs$/10^6 -$ pix /sec (four snowballs per group). Although the fluxes are small and the variations are relatively large, there appears to be a steady downward trend in the median flux of the snowballs as Cycles 1 and 2 progress, similar to the long-term decrease in the CR flux. In the early part of Cycle 1, up to about January 2023, the median flux of snowballs is most commonly 4.476×10^{-2} snowballs$/10^6 -$ pix /sec (two snowballs per group) while in the latter part of Cycle 2, it is uniformly 2.238×10^{-2} snowballs$/10^6 -$ pix /sec (one snowball per group).

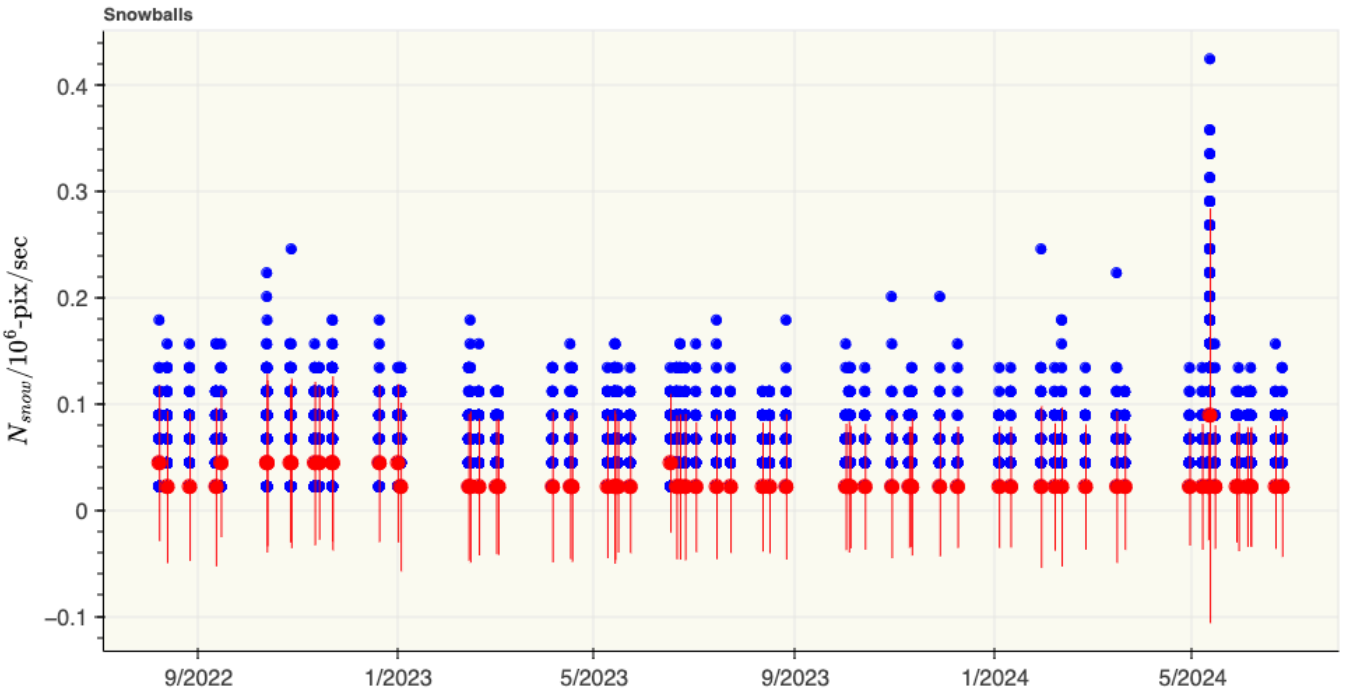

Figure 6-6. Same as Fig. 6-1 but for the snowballs. Groups with no snowballs are excluded.

Lastly, the flux of the CR trails is plotted in Fig. 6-7. As expected, the flux of trails decreases in a similar fashion as the CRs, about 40% from the beginning of Cycle 1 to the end of Cycle 2, 5.371×10^{-4} trails$/10^3 -$ pix /sec (24 trails per group) to 3.133×10^{-4} trails$/10^3 -$ pix /sec (14 trails per group).

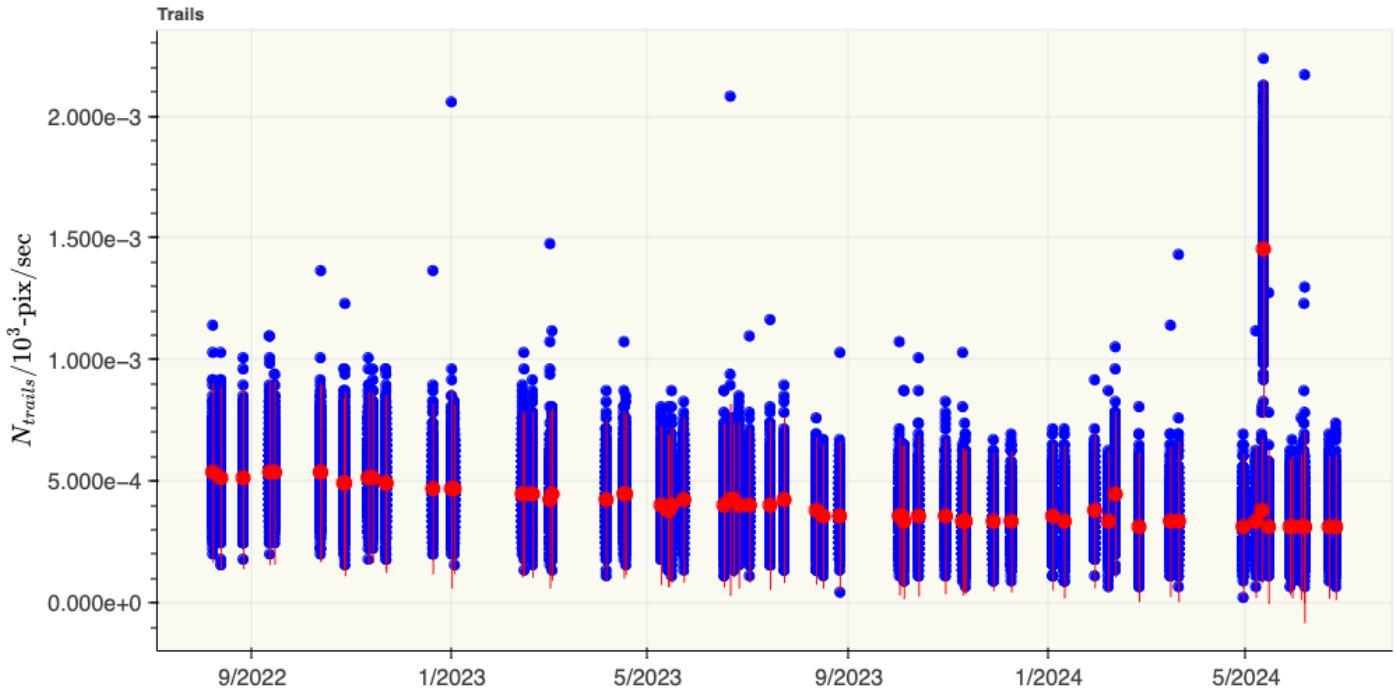

Figure 6-7. Same as Fig. 6-1 but for the trails.

6.2 Spatial Distribution of the CRs

There are typically a few hundreds of CRs in each group of the dark exposures. Their location and distribution on the detector may offer clues to their origin and arrival times. Here, we apply quadrat statistics to test the null hypothesis that the spatial distribution of the CRs over the detector is random. To do so, the Python module *pointpats*, a subpackage of the Python Spatial Analysis Library (PySAL) (Rey & Anselin 2007), is used with the assumptions of uniformity (each location on the detector has an equal probability of being impacted by a CR) and independence (the locations of the CRs are independent of each other). The CRs are treated as a planar point pattern, i.e., only their coordinates are considered and no weight is given to their size or signal. A 4×4 rectangular tessellation is applied to each group of the integrations and the total number of CRs in each quadrat is calculated. By comparing the observed signal in each quadrat to their expected signal, the χ^2 statistic is calculated and the p-value is derived. A small p-value ($p < 0.05$) indicates that the null hypothesis can be rejected at the 95% confidence level, i.e., the spatial distribution of the CRs is not random.

In Figs 6-8 and 6-9, examples of random and non-random spatial distributions of the CRs in the dark exposure of 1497:29 are shown. In the two panels of Fig. 6-8, the CRs are evenly distributed over the detector area. But in the more extreme examples of Fig. 6-9, they are heavily clumped in the bottom half of the detector (left panel) or elongated in a narrow "jet" in the top-left corner (right panel). Moreover, the groups with a non-random spatial distribution of CRs possess an excess of CRs compared to the groups with random distributions. This is apparent in the examples of Fig. 6-9, where the number of CRs is about two or three times the numbers in the panels of Fig. 6-8. To further highlight these differences further, a boxplot of the flux of the CRs in this exposure is shown in Fig. 6-10. The median flux of CRs with a non-random spatial distribution is 3% greater than its random counterpart. But more importantly, the flux of CRs in

the non-random spatial distribution span a much larger range. In fact, the excess flux of CRs observed in specific groups, such as shown in Fig. 6-2, can be directly attributed to these clumps of CRs. These results are typical of all the dark exposures.

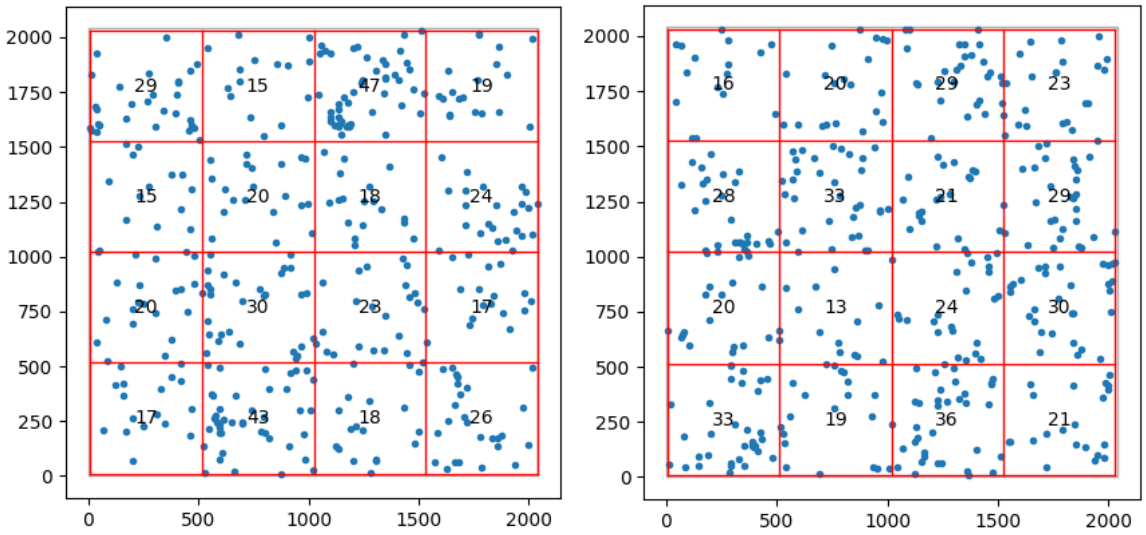

Figure 6-8. The quadrats of random distributions of CRs are shown for two groups (integration 2, groups 48 and 105 of 1497:29). The number of CRs in each quadrat are shown.

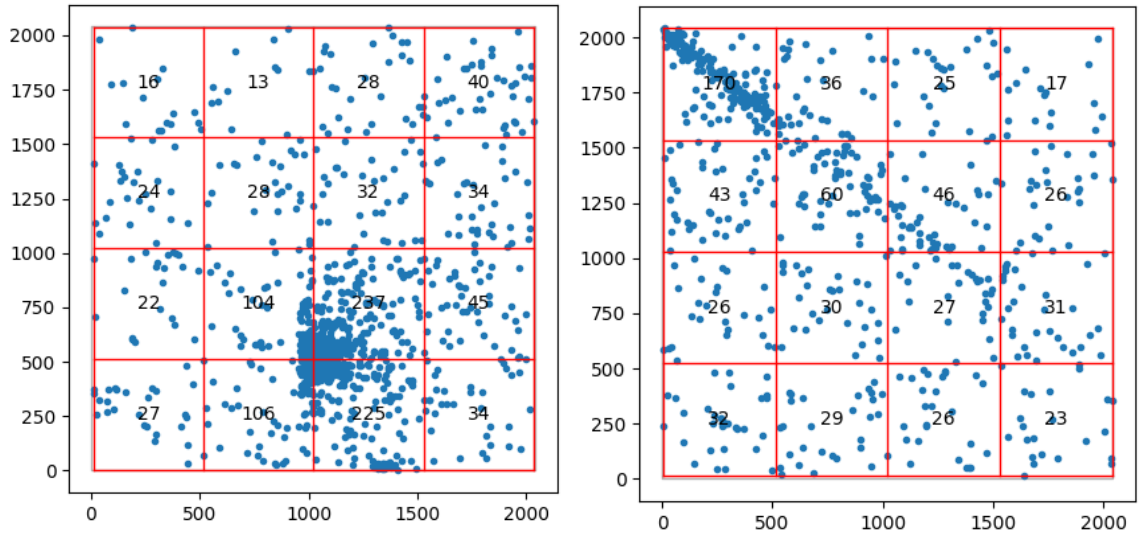

Figure 6-9. Same as Fig. 6-8 but for non-random distributions of CRs ($p < 0.05$) (integration 4, group 120 and integration 5, group 88 of 1497:29).

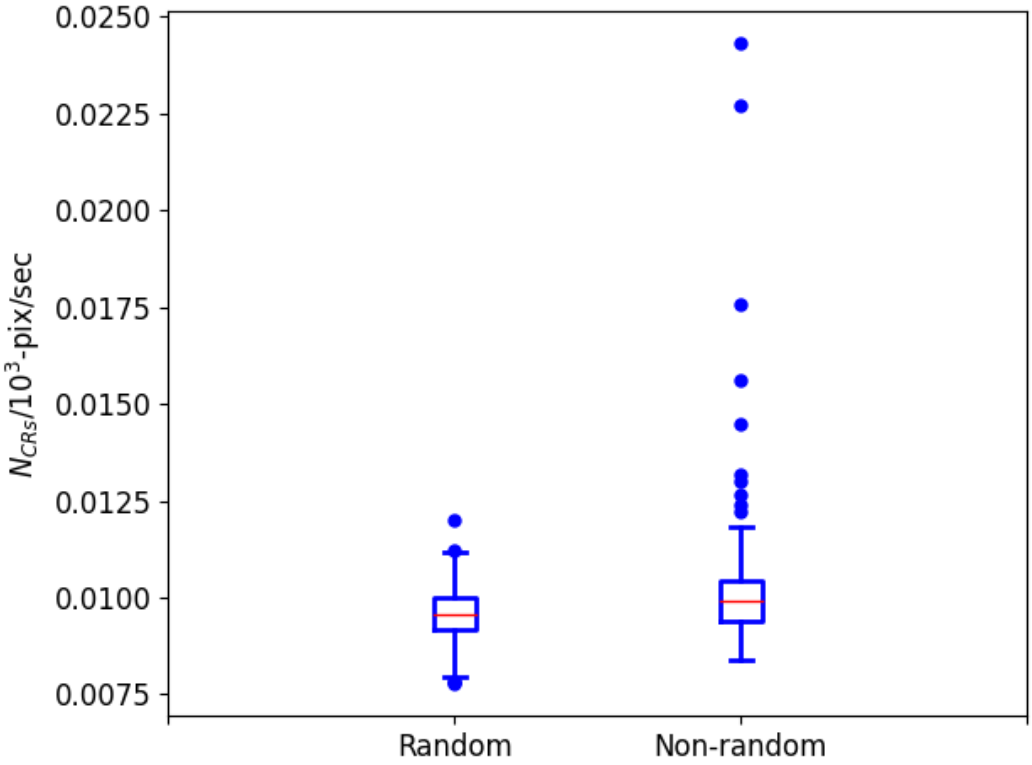

Figure 6-10. Boxplots of the flux of CRs with random and non-random spatial distributions in the exposure of 1497:29. The box extends from the first quartile (Q1) to the third quartile (Q3) of the data with a red horizontal line at the median. The whiskers extend from the box to the farthest data point lying within $1.5\times$ the inter-quartile range (IQR) from the box. The outliers (circles) extend past the end of the whiskers.

Over the course of Cycles 1 and 2, the number of groups with non-random spatial distributions of CRs has also increased significantly. This is shown in Fig. 6-11 where the fraction of groups (in percent) with $p < 0.05$ in each dark exposure is plotted. At the beginning of Cycle 1, approximately 33% of the groups of the exposures had such spatial distributions of CRs but by the end of Cycle 2, that number had reached 41%. Again, the dark of 4473:35 (2024-05-11), which possesses unusually large fluxes of CRs and snowballs (Section 6.1), is a clear outlier – only 15% of its groups have CRs with non-random distributions on the detector.

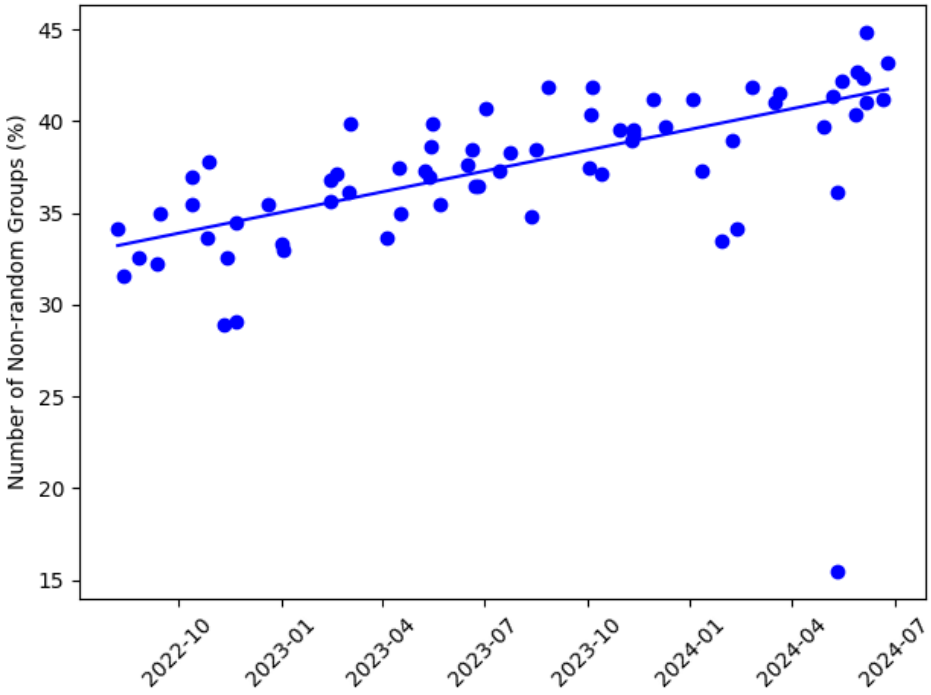

Figure 6-11. The percentage of groups with non-random distributions of CRs in each exposure is shown. The blue line represents a linear fit to the data points.

When visually inspecting the snowballs in individual groups of an exposure, it became apparent that some are surrounded by an excess of CRs. To investigate this further, we calculate the number of CRs inside an annulus of 100 pixels around snowballs of a wide range of sizes (25 – 200 pixels) and compare the numbers to a control sample of CRs that are four pixels in size or greater. The analysis is performed on groups with a random spatial distribution of CRs (Section 6.2) to avoid any bias from large clumps of excess CRs. Only the snowballs with annuli that do not overlap and that do not extend past the edge of the imaging area of the detector are included in the sample. For direct comparison, 200 CRs are selected in the same groups and those with annuli that overlap with those of the snowballs or other CRs or that extend beyond the edge of the detector are rejected. In total, the samples consist of ≈ 21100 and $\approx 2.89 \times 10^6$ CRs that surround the snowballs and other CRs, respectively, for all the dark exposures.

In Fig. 6-12, the distributions of the number of CRs that surround the smaller snowballs (size of 25 – 100 pixels) with those that surround the CRs are compared. Both the snowballs and CRs are predominantly surrounded by ≈ 3 CRs. But the snowballs are surrounded by a larger number of CRs over the range of $\approx 5 - 14$ CRs, while the CRs show an excess of a small number of neighboring CRs, $\approx 1 - 2$ CRs. To determine if the two distributions are statistically different, we apply the χ^2 test with the null hypothesis that there is no significant difference between the two distributions. We find a p-value much smaller than the significance level of 0.05, so the null hypothesis is rejected and we conclude that the two distributions are significantly different. Similarly, in Fig. 6-13, we compare the distributions of the number of CRs around snowballs of various sizes: $25 - 100$ pixels, $100 - 150$ pixels, and $150 - 200$ pixels. Again, the larger snowballs possess an excess of nearby CRs compared to their smaller counterparts. The χ^2 test again shows that the three distributions are significantly different.

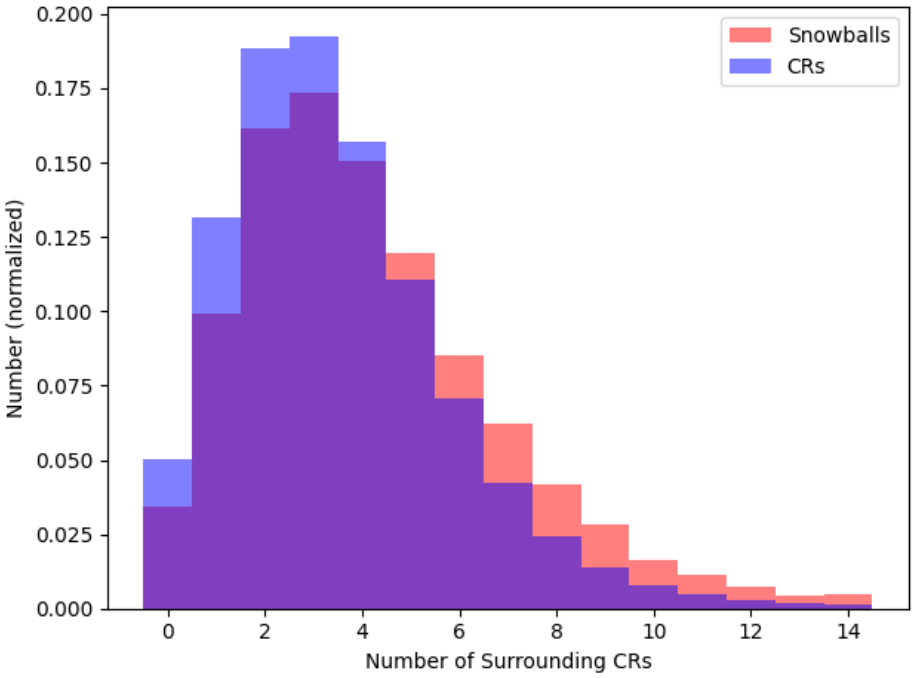

Figure 6-12. The distributions of the number of CRs surrounding snowballs of size 25 – 100 pixels (red) and other CRs (blue) are shown. The total area under each histogram is normalized to a value of one.

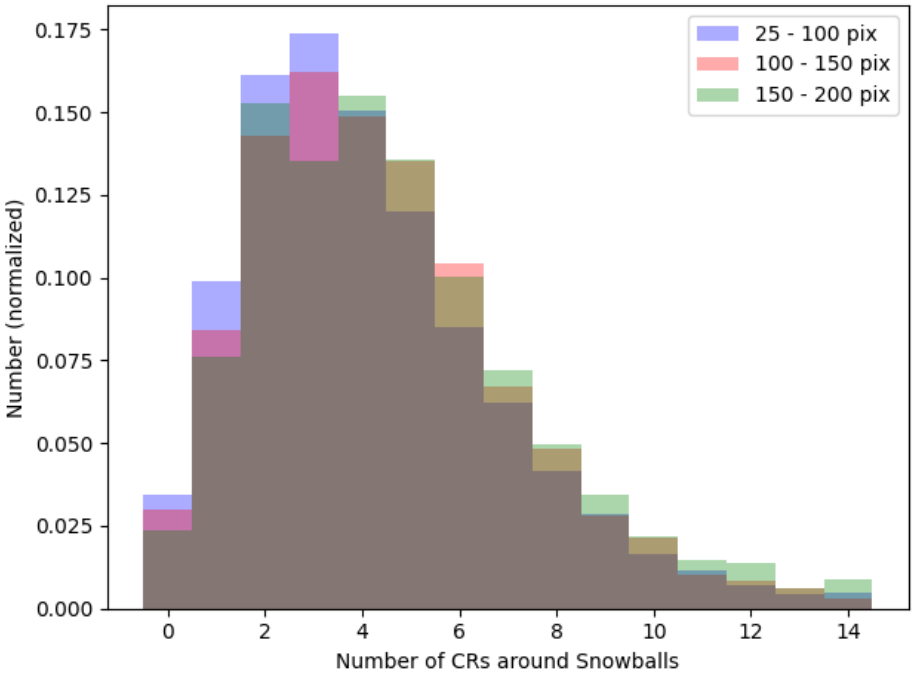

Figure 6-13. The distributions of the number of CRs surrounding snowballs of various sizes are shown. The total area under each histogram is normalized to a value of one.

6.3 Solar Activity and the Flux of CRs in NIRISS

We compare the long- and short-term trends of the CRs detected on the NIRISS detector with the proton fluxes measured directly by dedicated space weather instruments. Although there are several space observatories that monitor solar activity, we choose the latest iteration of the Geostationary Operational Environmental Satellites, GOES-18 (or GOES), and the Advanced Composition Explorer (ACE) (Stone et al. 1998a) since they offer nearly continuous coverage over the period of our observations and also provide easily available online data in convenient formats. The Solar and Galactic Proton Sensor (SGPS) on GOES-18 measures solar and Galactic protons present within the Earth's magnetosphere at five-minute intervals over kinetic energies of $1 - 500$ MeV in thirteen differential channels and > 500 MeV in an integral channel. The Solar Isotope Spectrometer (SIS; Stone et al. 1998b) aboard ACE, located at L1, measures the isotopic composition of energetic nuclei from He to Ni over the energy range of from $\sim 10 - 100$ MeV/nucleon at five-minute intervals. These measurements may suffer from significant noise from higher-energy background particles. The bulk speed of the solar wind is measured by the Solar Wind Electron Proton Alpha Monitor (SWEPAM) (McComas et al. 1998), also aboard ACE.

The Level 2 data are issued daily as five-minute average fluxes by the Space Weather Prediction Center (SWPC) of the U.S. National Oceanic and Atmospheric Administration (NOAA). The SPGS files are in the NetCDF format which is handled with the Python module *netCDF4* while the SIS files are in simple text format. For the years 2022 to 2024, the SGPS data can be downloaded directly from https://data.ngdc.noaa.gov/platforms/solar-space-observing-satellites/goes/goes18/l2/data/sgps-l2-avg5m/ while the SIS data are available at https://sohoftp.nascom.nasa.gov/sdb/goes/ace/daily/ for the years 2001 to 2024.

6.3.1 Long-term Correlations

The GOES and ACE observatories offer continuous long-term monitoring of the proton fluxes as the solar cycle progresses. In Fig. 6-14, we show the SGPS fluxes of protons with energies > 500 MeV over most of the period when the darks of PIDs 1497 and 4473 were collected. This channel primarily measures the high-energy GCRs (Kress et al. 2021). There is an evident decrease in the fluxes by about 36%, i.e., ≈ 0.275 to ≈ 0.175 protons/(cm^2 sec sr), throughout this period including a flattening of the flux levels around January 2024. This behavior is expected as Solar Cycle 25 approaches its maximum activity sometime between January and October 2024 as predicted by SWPC (see press release of October 2023; https://www.weather.gov/news/102523-solar-cycle-25-update). The large "spike" in the SGPS fluxes on 2024-05-11 will be discussed in detail in the following section.

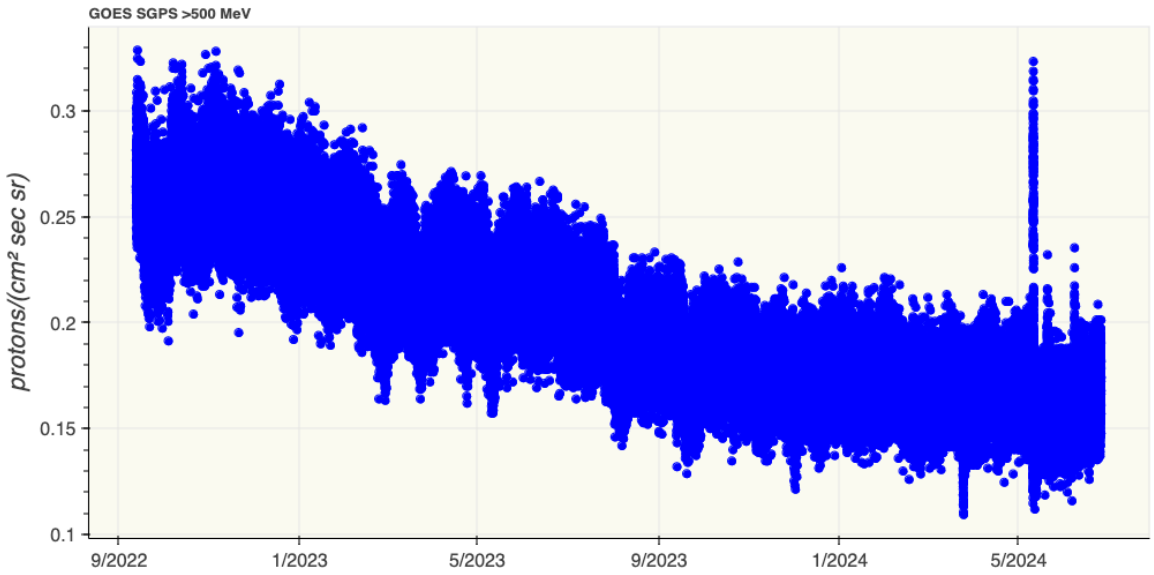

Figure 6-14. The SGPS proton fluxes with integral energies > 500 MeV are shown. The data are only available for dates of Sep 13, 2022 and later.

As presented in Section 6.1, the flux of the CRs measured by NIRISS declines with a very similar profile and amount, ≈ 35%. This is further illustrated in Fig. 6-15, where a strong linear correlation between the flux of GCRs measured by SGPS and the median flux of CRs measured by NIRISS (excluding the darks of 4473:25, 4473:31, and 4473:35) is found. These results therefore indicate that the NIRISS detector is highly sensitive to the background flux of energetic GCRs and the overall decrease in the flux of CRs in the dark exposures can be largely attributed to the natural progression of the solar cycle towards peak activity.

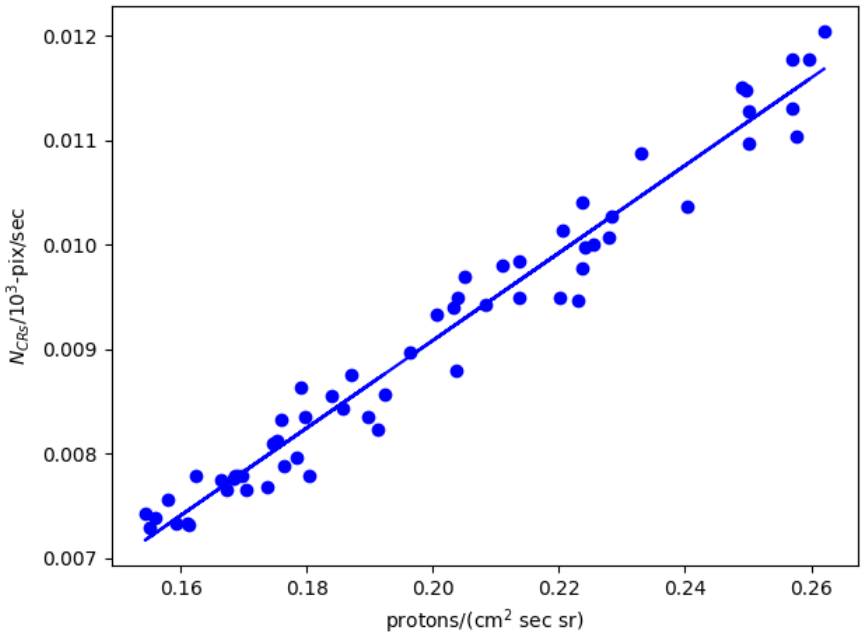

Figure 6-15. The flux of the NIRISS CRs is plotted against the GOES SGPS high-energy flux (> 500 MeV).

The decline in the proton fluxes measured by SGPS and in the CR hits impacting the dark exposures of NIRISS is also seen in the low-energy bands of SIS. Fig. 6-16 shows the SIS integral fluxes of > 10 MeV and > 30 MeV. The low-flux background is enlarged in Fig. 6-17. Although there are many discrete events with large fluxes caused by SPEs with durations of ≈ 2 days or so, there is a general decline in the overall low-level background. The decline is about 42%, roughly consistent with the results found for SPGS and NIRISS. If only the darks with reliable background SIS fluxes are considered, then we again find a linear relationship between the NIRISS CR fluxes and the SIS fluxes, as demonstrated in Fig. 6.18.

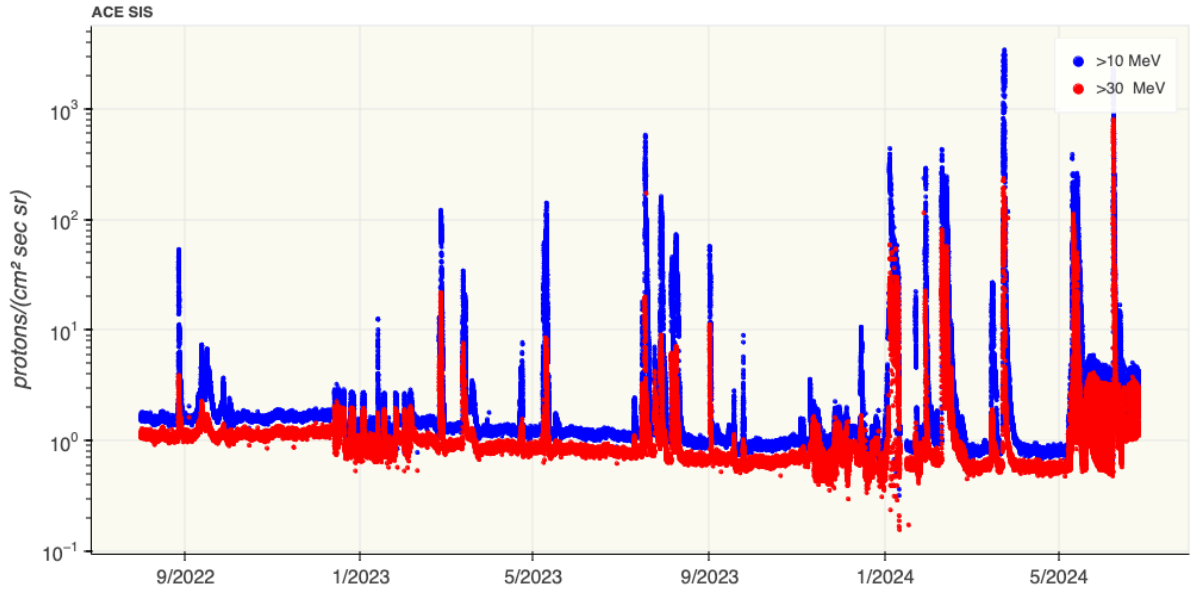

Figure 6-16. The SIS integral proton fluxes for energies of > 10 MeV and > 30 MeV are shown.

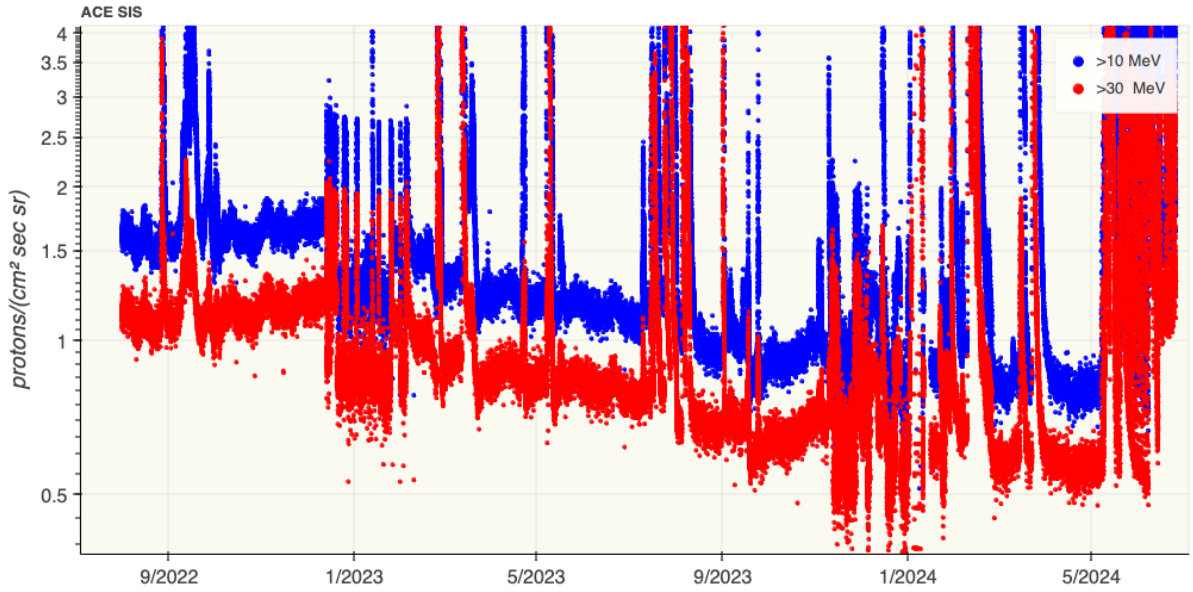

Figure 6-17. Enlargement of Fig. 6-16 showing the decline in the proton background.

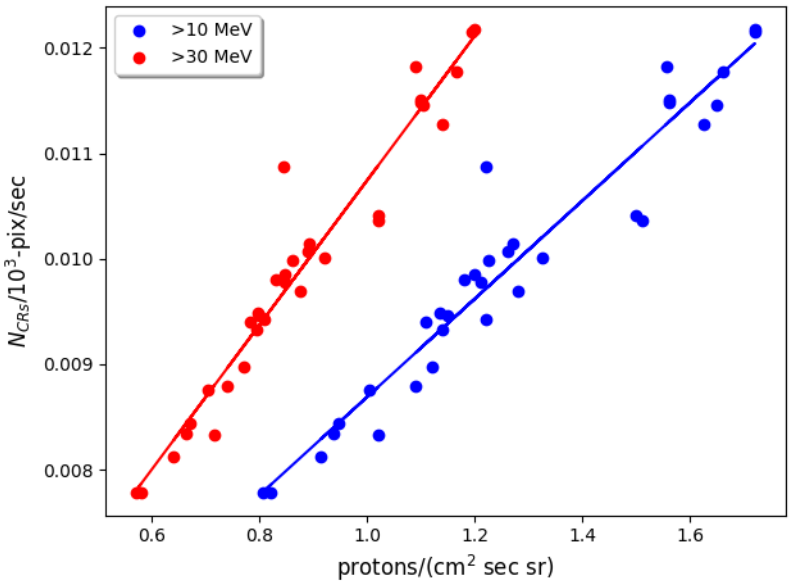

Figure 6-18. The flux of the NIRISS CRs is plotted against the ACE SIS fluxes (> 10 MeV, > 30 MeV).

The anti-correlation between the background flux of CRs in NIRISS and the solar activity is further demonstrated in Fig. 6-19 where the number of sunspots recorded by the Sunspot Index and Long-term Solar Observations (SILSO World Data Center) is plotted from the last solar minimum in Dec 2019 to June 2024. As expected, as the number of sunspots increases, the CR flux in NIRISS decreases. The largest number of sunspots occurred in May 2024, the month that saw unusually powerful solar storms that produced the large spike in the number of CRs in the dark of 4473:35 (2024-05-11).

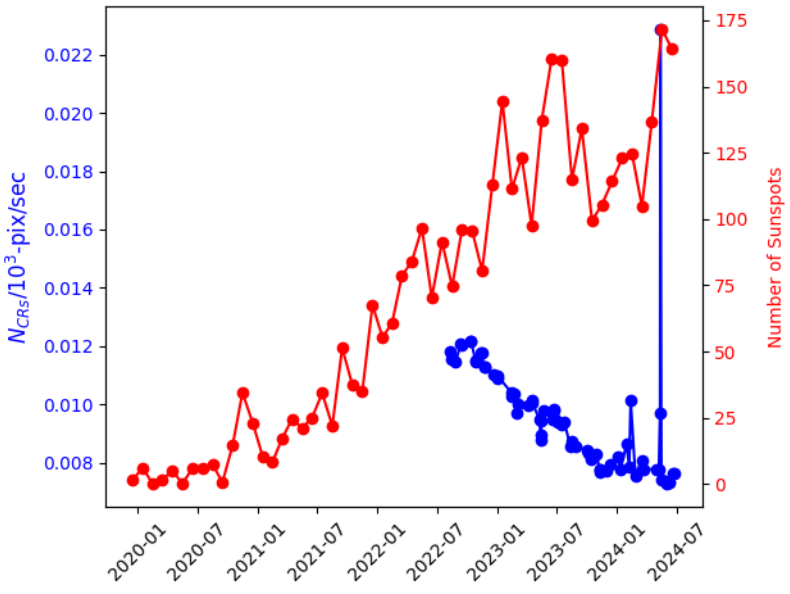

Figure 6-19. The median flux of CRs measured with NIRISS and the number of sunspots since the last solar minimum in Dec 2019 are shown in blue and red, respectively. The large flux of CRs in the dark of 4473:35 matches the highest number of sunspots in May 2024.

6.3.2 Short-term Correlations

In the previous section, we found that the overall declining flux of the CRs correlates with the background flux measured by the GOES and ACE satellites over the 2-year period our dark exposures were collected. Although the majority of the darks were acquired in relatively quiescent periods of solar activity, three darks show elevated and variable CR fluxes on the short timescale of their 2-hour duration: 4473:25, 4473:31, and 4473:35, as discussed in Section 6.1. Were these darks coincident with periods of unusually high solar activity? To investigate this possibility, we compare the date and time of these darks with the differential fluxes of SGPS and the integral proton fluxes measured by SIS.

In Fig. 6-20, we plot the fluxes of the NIRISS CRs, the SGPS differential fluxes, and the SIS integral fluxes over an interval of about 3.5 days surrounding the acquisition of the dark of 4473:25 (2024-02-11). The mean bulk speed of the solar wind measured by the SWEPAM instrument on ACE was roughly 400 km/s over the two hours preceding this dark. The delay between the flux measurements in SIS at L1 and NIRISS at L2 is therefore ≈ 2 hours and between SGPS in geosynchronous orbit and NIRISS, ≈ 1 hour. These delays are about the same duration (or less) than the dark and so for our purposes, no adjustments are made to the arrival times of the particles at the different observatories. We find that this dark was collected ≈ 1.5 days after the beginning of a significant solar event, as the high proton fluxes detected in the energy band of SGPS and in the integral bands of SIS attest. This event had a total duration of about nine days. The SGPS and SIS fluxes are up to $\approx 900\times$ and $\approx 210\times$ greater than their background levels at the time the dark was taken. We therefore conclude that the elevated flux of CRs in this dark as well as its unusual positive slope as the exposure progresses are caused by a powerful SPE.

The darks of 4473:31 and 4473:35 were acquired amidst a series of extreme solar geomagnetic storms from May 3 to May 13. Two active sunspot complexes labeled AR 13663 and AR 13664 produced highly energetic solar flares and launched CMEs towards the Earth that produced spectacular aurorae visible in southern latitudes. For the first time since October 2023, the SWPC classified some of these storms as G5 (Extreme Geomagnetic Storm) events. The solar wind speed of these storms was about $700 - 900$ km/s. As expected, from Fig. 6-21, the large fluxes of CRs in NIRISS are coincident with large particle fluxes in the energy bands of SGPS and SIS. In fact, some of the highest fluxes measured in these instruments occurred during this short time period. The "spike" observed in the high-energy band (> 500 MeV) of SGPS on 2024-05-11, enlarged in Fig. 6-22, can be attributed to these extreme G5 storms. Some of the particles were so energetic that they briefly dominated this high-energy band, well above the background of the GCRs. The increase in the snowball fluxes in these two darks indicates that some snowballs originate from particles ejected in solar storms.

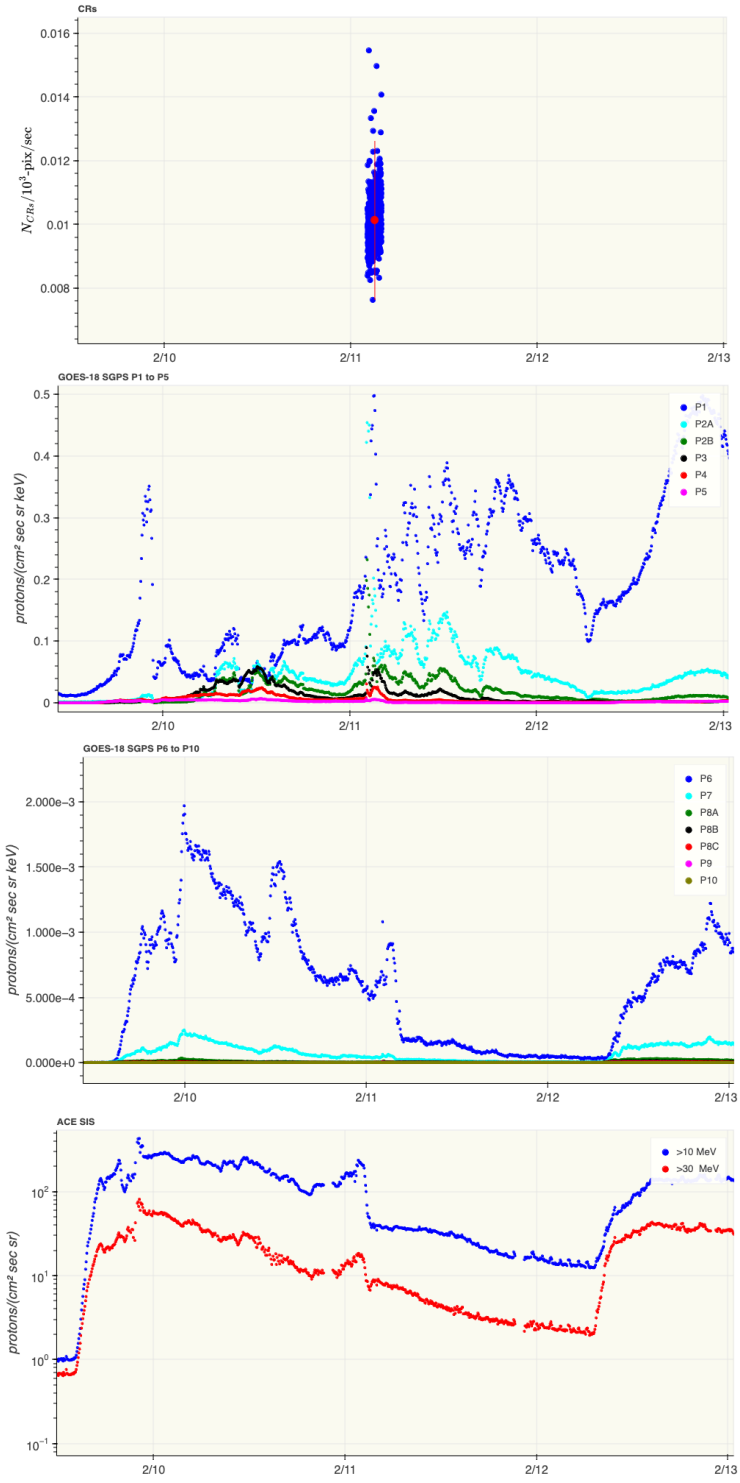

Figure 6-20. First panel: The flux of CRs in the dark exposure of 4473:25 (2024-02-11). Second panel: The SGPS fluxes in the energy bands P1: $1-1.9$ MeV, P2A: $1.9-2.3$ MeV, P2B: $2.3-3.4$ MeV, P3: $3.4-6.5$ MeV, P4: $6.5-12$ MeV, P5: $12-25$ MeV. Third panel: The SGPS fluxes in the energy bands P6: $25-40$ MeV, P7: $40-80$ MeV, P8A: $83-99$ MeV, P8B: $99-118$ MeV, P9: $150-275$ MeV, P10: $275-500$ MeV. Bottom panel: The SIS fluxes at integrated energies of >10 MeV and >30 MeV.

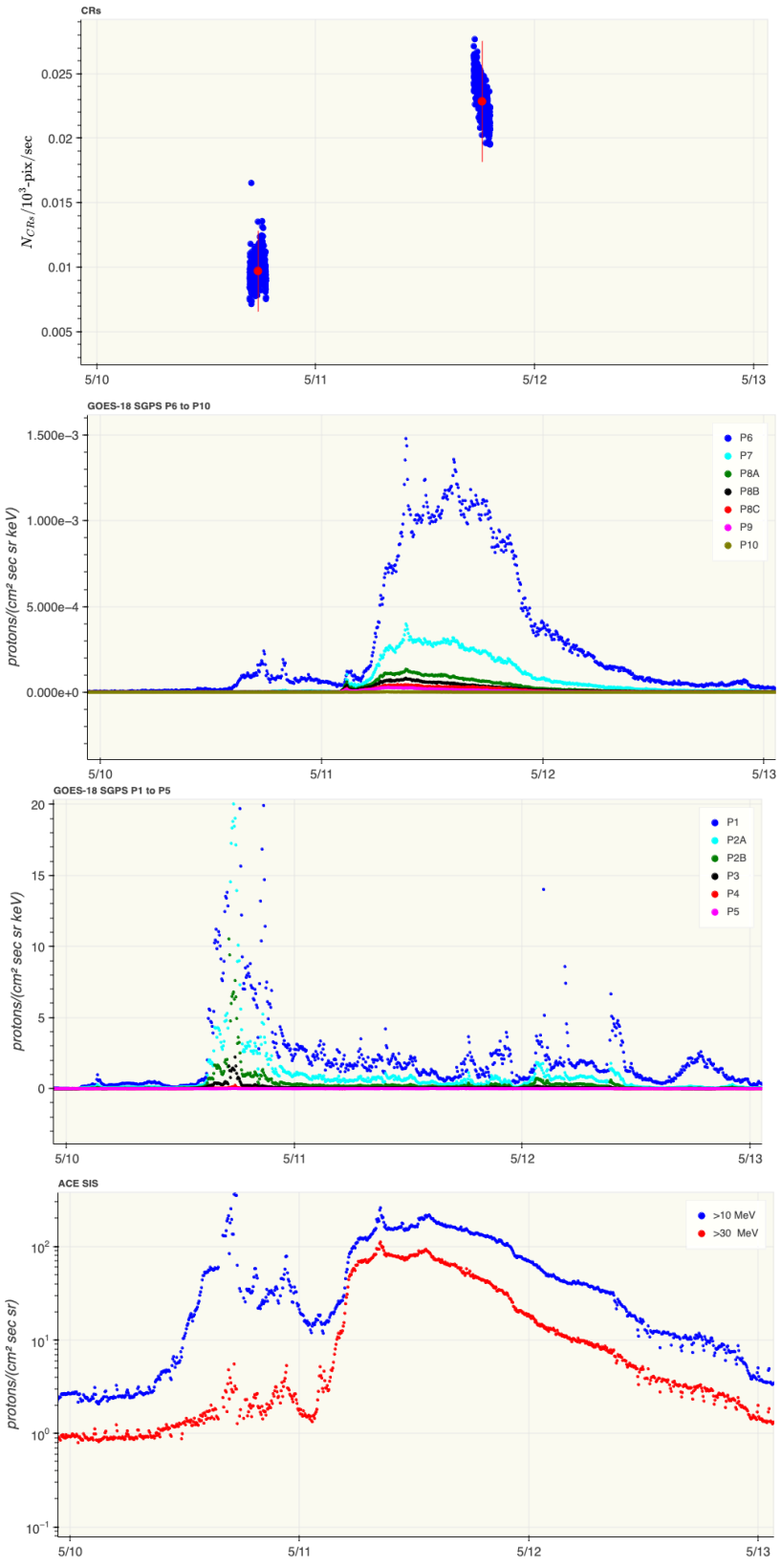

Figure 6-21. Same as Fig. 6-20 but for the darks of 4473:31 (2024-05-10) and 4473:35 (2024-05-11).

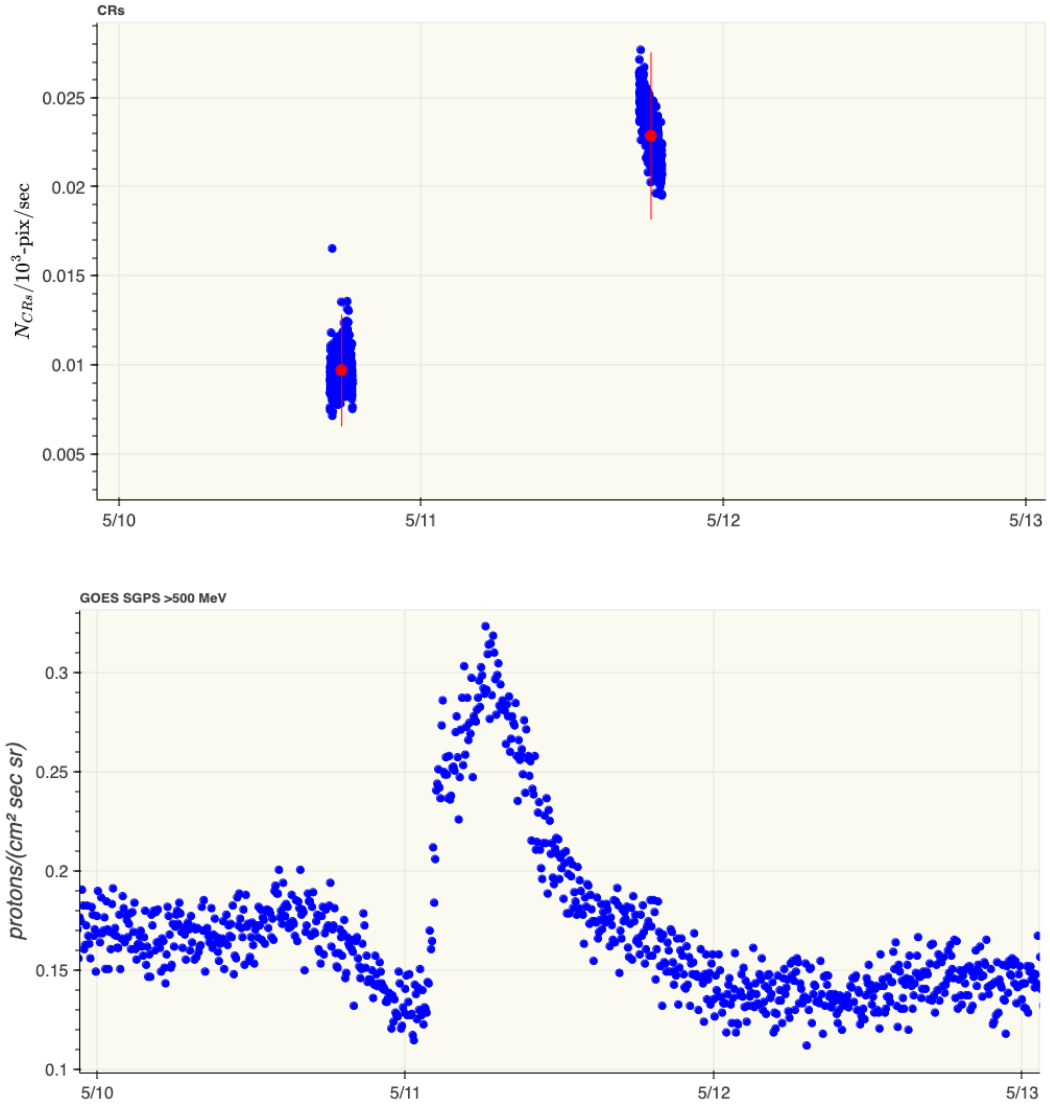

Figure 6-22. Top panel: The flux of CRs in the darks of 4473:31 (2024-05-10) and 4473:35 (2024-05-11). Bottom panel: Enlargement of the flux spike in Fig. 6-14 on 2024-05-11. Its duration is approximately one day.

In Section 6.2, we established that some groups of the NIRISS dark exposures possess a large excess of CRs that are not randomly distributed over the area of the detector, i.e., showers, clumps, and jets. We do not find a strong correlation between a single group of a NIRISS exposure and an increase in the SGPS or SIS flux. This negative result is due to the long duration of days or hours of the events recorded by SGPS and SIS at a relatively coarse resolution in time of five minutes, significantly longer than the 10.7 sec duration of a NIRISS group. It is also not evident from our data if any anomalous trend in the flux of CRs in the NIRISS darks correlates more strongly with the SGPS or SIS fluxes (or both). Undoubtedly, the different locations of the three observatories in space, the geometry and orientation of their orbits, and the shielding around the NIRISS detector likely play an important role in the timing and coincidence of the solar particles on their detectors.

6.4 Impact of CRs on the Dark Count Rates and Bias Levels

For a constant FPA temperature, the basic properties of the NIRISS detector should show very little or no change over the duration of the mission. This stability is crucial for the NIRISS science observations and alleviates the need to frequently update the calibration reference files. It is therefore important to determine if the CRs have any impact on the detector's long-term performance. To do so, we calculate two important properties of the detector over time, the dark rate and the "bias" level. The raw dark exposures were re-processed as described in Section 4 but with the default value of 90 sec for the parameter *after_jump_flag_time_1* to ensure that the slopes calculated after the group of a CR hit are not biased in any way (but the value of this parameter made no difference to the results). All the other step parameters and reference files were unchanged.

In Fig. 6-23, a typical dark rate image is displayed. The large void near the center of the detector as well as the smaller voids in the upper part are due to missing epoxy between the silicon ROIC and the HgCdTe detector layer (Rauscher 2015). The voids represent about 20% of the detector area. Other than a lower gain, dark rate, and interpixel capacitance (IPC), the pixels inside the voids generally behave like those outside of them. The bright horizontal line at the center of the detector (Y = 1024 pix) and the small, bright patch in the top-right corner are due to amplifier glow. The bright feature at Y = 1536 pix along the left edge is a known detector defect.

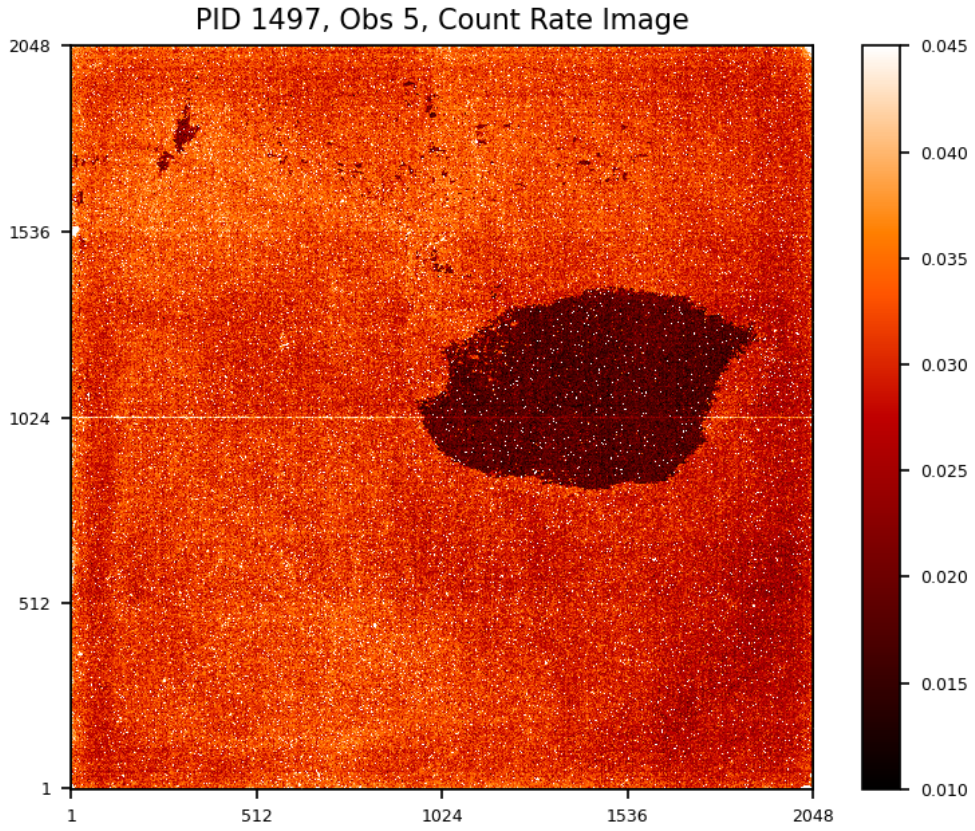

Figure 6-23. Dark rate image of 1497:5 (NINTS = 5, NGROUPS = 120). The units are ADU/sec.

The median count rates inside and outside the void are plotted in Fig. 6-24. Bad pixels flagged with a value of DQ = 1 (DO_NOT_USE) as well as saturated pixels with DQ = 2 (SATURATED) were excluded from the calculations. A 2nd-order polynomial is fit to each curve. The vertical lines indicate when the NIRISS power was cycled in Cycles 1 and 2. These four instances of restoring NIRISS to normal operations do not appear to have altered the overall trend. The dark of 4473:35 (2024-05-11), acquired during a period of extreme solar activity, shows an anomalously large dark rate, both inside and outside the void. Overall, the dark rate declines significantly by ≈ 12% and ≈ 7% inside and outside the void, respectively, over the 2-year period of data collection. There is a slight flattening starting around January 2024 as seen above for the flux of CRs.

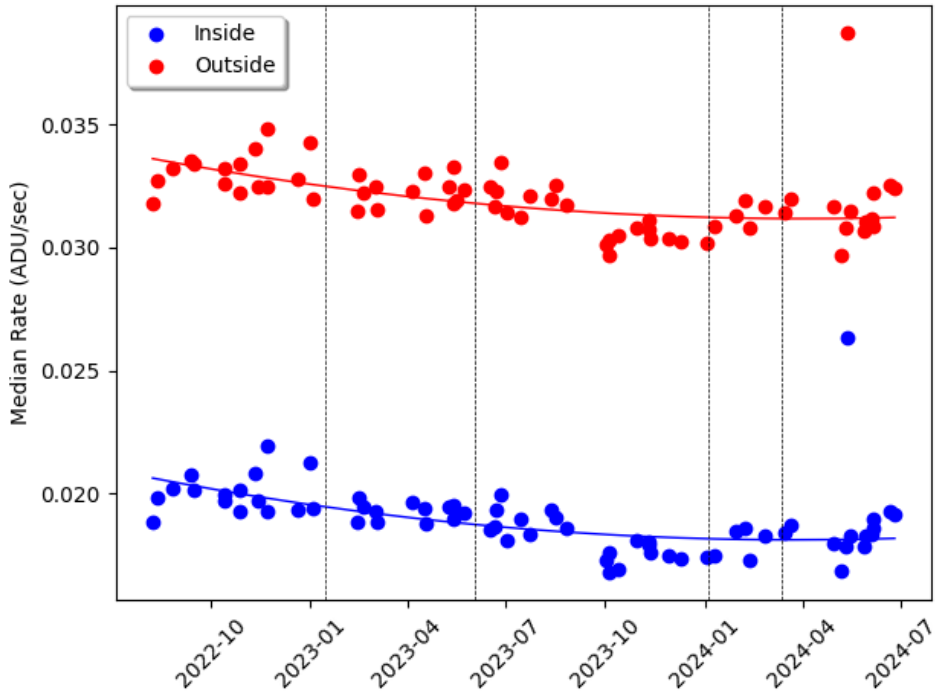

Figure 6-24. The median count rates inside and outside the void of each dark are plotted. The solid lines represent 2nd-order polynomial fits. The dashed vertical lines indicate when NIRISS was powered off and on (Jan 15, 2023; Jun 1, 2023; Jan 4, 2024; Mar 12, 2024).

This steady decline and flattening of the dark rate are reminiscent of those of the flux of CRs in the NIRISS detector as the solar cycle progresses. Indeed, as Fig. 6-25 shows, the dark rate correlates linearly with the flux of CRs, even for the outstanding dark rate of 4473:35. Above, we showed that the flux of NIRISS CRs and the GOES SGPS high-energy particle flux (> 500 MeV) are correlated and so, as expected, in Fig. 6-26, the dark rate also correlates with this SGPS high-energy flux. The large spike of the SGPS flux and the dark of 4473:35 are not quite coincident in time (see Fig. 6-22), which may explain why this data point is an outlier in this figure.

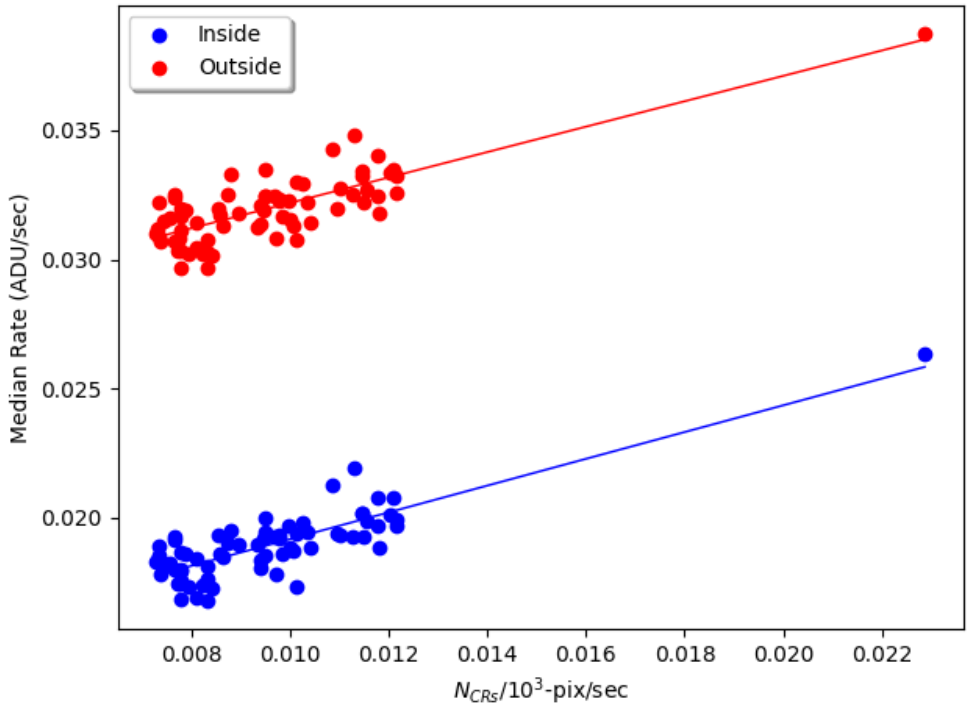

Figure 6-25. The dark rates inside and outside the void are plotted against the flux of the NIRISS CRs. The solid lines represent linear fits.

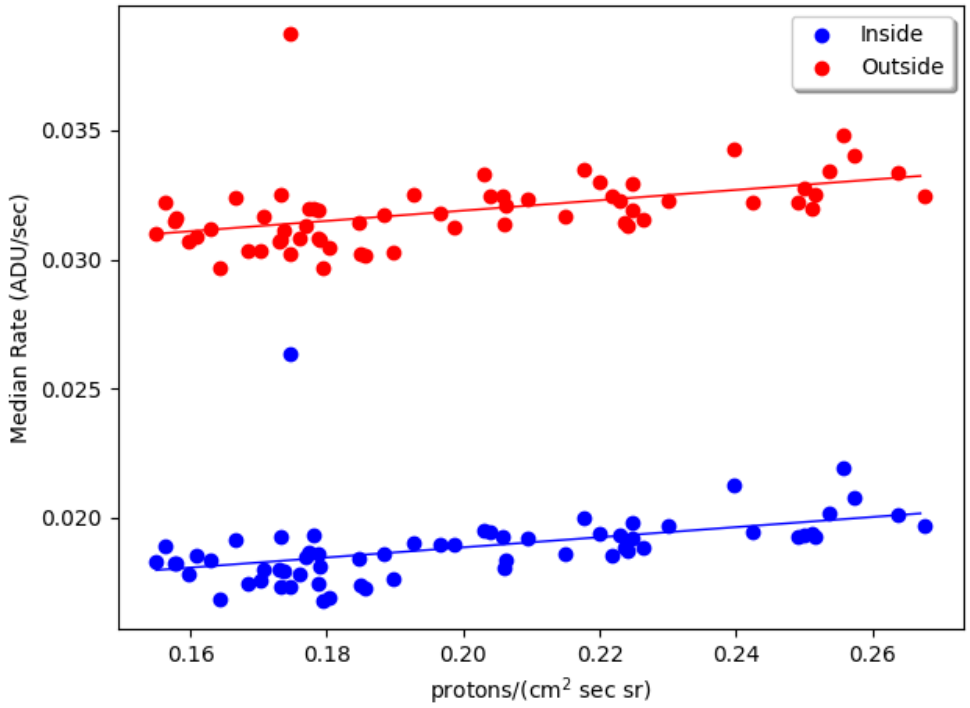

Figure 6-26. The dark rates inside and outside the void are plotted against the GOES SGPS high-energy flux (> 500 MeV). The solid lines represent linear fits.

The analysis of dark exposures collected in the pre-launch characterization of the detector and in the activities at cryogenic temperatures revealed that the dark signal of the NIRISS detector is dominated by a near constant "glow" or "flash" from the readout electronics in both full-frame and subarray exposures (in ADU/frame). Our results therefore indicate that the CRs produce an additional, slowly variable signal atop this constant component. The true value of this electronic glow can be measured when the CR flux is at a minimum. From Fig. 6-24, we find a glow rate of about 0.0182 ADU/sec (0.195 ADU/frame) and 0.0312 ADU/sec (0.335 ADU/sec) inside and outside the void, respectively, for the full frames.

We repeat the same analysis for the count levels of the first group of each ramp exposure, which we call the bias level. The median count levels of the imaging area of the first group of the five integrations were measured and the mean of these five values was then calculated. The values are plotted in Fig. 6-27. Again, the overall trend in the bias level appears to follow the behavior of the flux of CRs over this time span – a relatively steep decrease in signal leading into a more gradual decline. The total decrease over this time period is about 30 ADUs per pixel. We reiterate that all the exposures were processed with the same superbias reference file (*jwst_niriss_superbias_0183.fits*) created early in the mission from darks acquired in the commissioning program PID 1081. Clearly, this superbias slightly over subtracts the decreasing bias level in the later Cycle 1 and 2 darks.

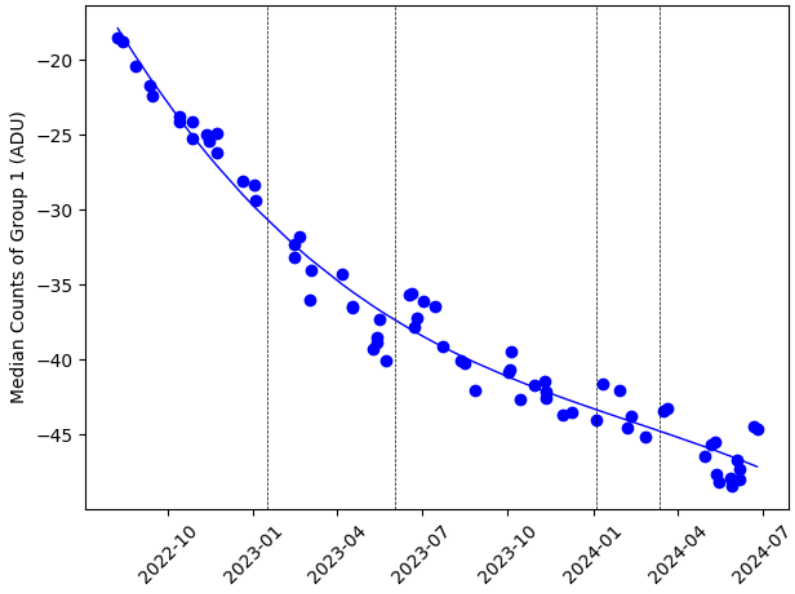

Figure 6-27. The bias level of the exposures is plotted. The solid line is a 3rd-order polynomial fit. The dashed vertical lines indicate when NIRISS was powered off and on (Jan 15, 2023; Jun 1, 2023; Jan 4, 2024; Mar 12, 2024).

From Figs 6-28 and 6-29, the bias level correlates linearly with both the flux of CRs on the NIRISS detector and the GOES SGPS high-energy flux (> 500 MeV). In general, the higher the CR flux, the higher the bias level. But curiously, the dark with the highest CR flux, 4473:35, does not show an elevated bias level. This may indicate that the correlation of the bias level with the CR flux is misleading, and potentially a red herring, and that another factor is dominating the trends. It will be necessary to follow the evolution of the bias level through the entire solar cycle to fully understand and confirm the cause of these correlations.

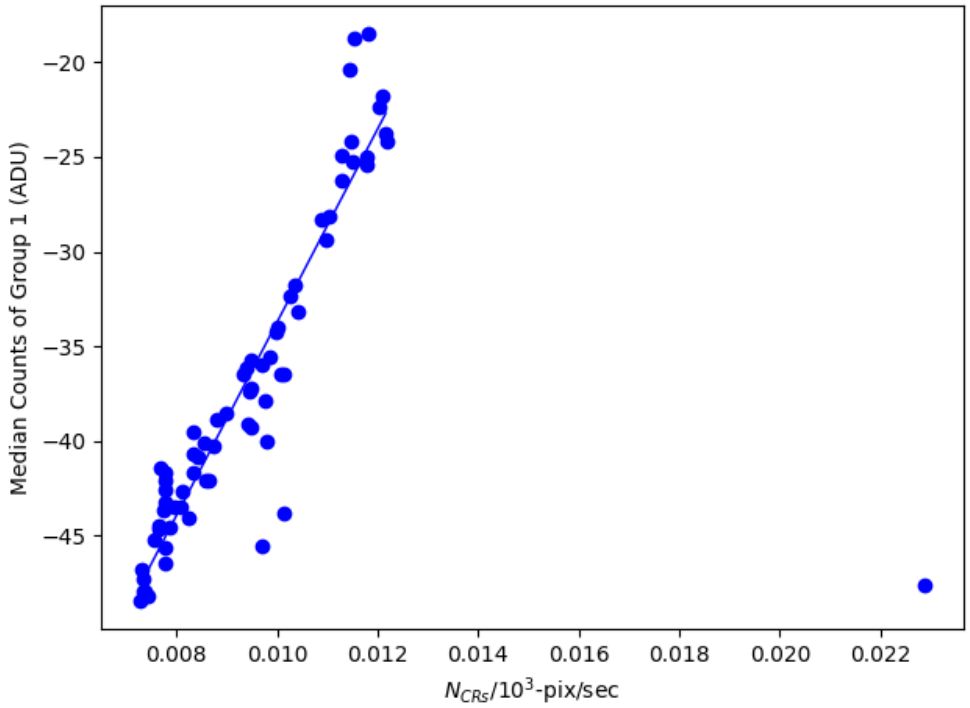

Figure 6-28. The bias level is plotted against the flux of the NIRISS CRs. The solid line is a linear fit to all the bias levels except for the dark of 4473:35.

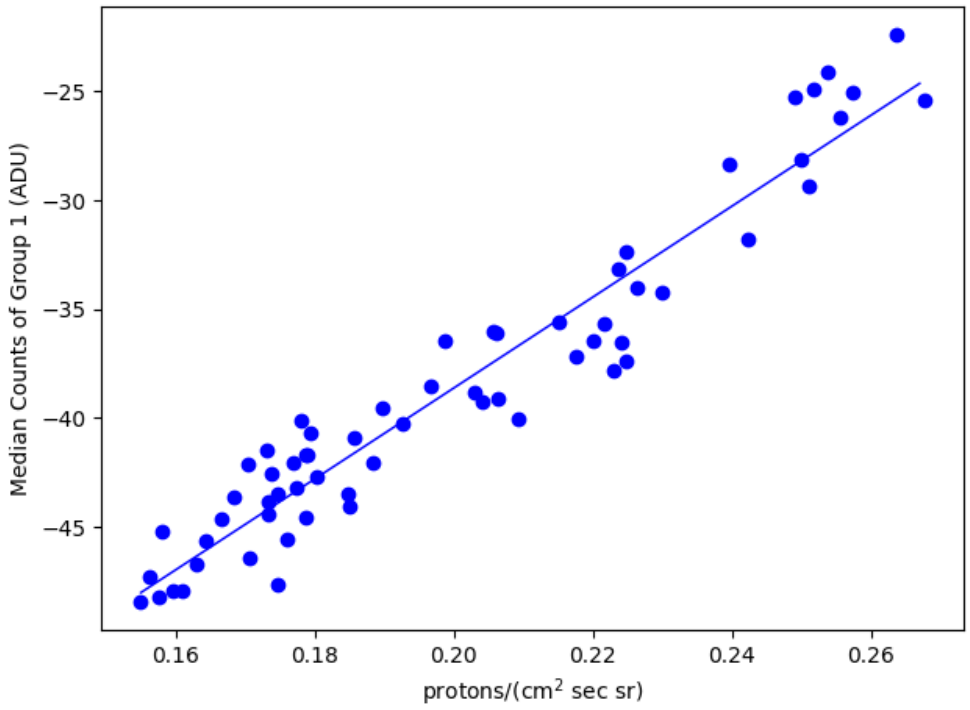

Figure 6-29. The bias level is plotted against the GOES SGPS high-energy flux (> 500 MeV). The solid line is a linear fit.

7 Discussion

The fluxes of the CRs and snowballs in the deep full-frame dark exposures of NIRISS are correlated with the progression of the solar cycle. Throughout Cycles 1 and 2, the flux of the CRs decreased by approximately 35%. The rate of decline is not constant – it is steeper in the earliest months of observations, at the beginning of Cycle 1, and slowly levels off around January 2024, in the middle of Cycle 2. This long-term behavior of the particle background in NIRISS is consistent with the decline in the flux of GCRs entering the Solar System as the Sun enters a period of elevated activity at the peak of the solar cycle. This observation is supported by the linear relationship between the NIRISS CR flux and the background fluxes measured by the GOES SGPS and ACE SIS instruments in the Earth-Moon system. In principle, one could predict the NIRISS CR flux by simply correlating it with the publicly available SGPS and SIS fluxes. In addition to this declining background, some darks also show elevated fluxes of CRs, which can be attributed to short-duration SPEs and CMEs. Clusters, showers, and jets of CRs also become more frequent as the solar cycle approaches its peak.

The flux of snowballs also shows a decline as Cycles 1 and 2 progressed but the trend is not as pronounced as for the CRs. Although our analysis considered only the snowballs with circular morphologies, many also show significant elongations or trails. Their flux is also significantly higher than that of the snowballs observed in the ground test campaigns, indicating that the majority do not originate from radioactive decay in the HgCdTe detector, considering that the radioactive decay rate continuously decreases with time since the date of manufacture of the detector. We therefore conclude that the vast majority of the snowballs detected in the on-orbit exposures are cosmic/solar in origin. The excess of CRs surrounding the snowballs and the increase of their flux in some solar events lends further credence to an external origin.

The dark rate and the bias level of the NIRISS detector also appear to follow the same general trend as the flux of CRs, i.e., the larger the CR flux, the larger the dark rate and bias level. Low-energy CRs, which could go undetected and uncorrected in Stage 1 of the calibration pipeline, are most likely blocked by the shielding around the detector and are unlikely to be the source of these correlations. On the other hand, long-term, cumulative, and uniform persistence and/or short-term persistence between consecutive frames and integrations could contribute to the observed correlations (Pickel et al. 2004). The dark exposures should be reprocessed with systematic changes to the parameters of the jump detection algorithm, especially the rejection threshold, to evaluate the impact of the CR flux and persistence on the dark rate and bias levels.

The CRs could also indirectly produce additional signal in the detector. An optical element in the light path of NIRISS may be subject to photoluminescence, proportional to the proton energy deposited by the CRs on this surface. Such fluorescence has been suggested to explain a similar dependence of the dark current rate on the solar cycle in the WFC3 UVIS and WFPC2 instruments (Bourque & Baggett 2016). For WFPC2, the CCD windows were constructed with MgF2 and are believed to have been the source of the fluorescence. But there is no window in front of the NIRISS detector surface (Aldridge et al. 2007). An intriguing candidate for luminescence is the bandpass transmission coatings and anti-reflection (AR) coatings on the filters and the AR coating on the detector. Some of these coatings contain SiO_2, as described by Evans (2005) for the optical components of the Tunable Filter Imager (TFI), the first incarnation of NIRISS. This material is a known source of electron-induced luminescence (cathodoluminescence) (Evans Jensen et al. 2013), albeit primarily at visible wavelengths ($\lesssim$

1 μm). Further work would be required to determine if the flux of electrons in the plasma environment at L2 can explain our results, including modulation by the solar cycle.

For completeness, we mention two other potential but unlikely sources of luminescence. The CdZnTe substrate in some near-IR detectors can be susceptible to photoluminescence when exposed to CRs, e.g., Waczynski et al. (2005), and so the NIRISS detector was made without such a substrate (Rowlands et al. 2008). Additionally, all the detector assembly components (excluding the internal FPA parts and the SIDECAR package) are made of aluminum 6061-T6 to match the materials of the housing and baffle (Aldridge 2007). This 10-mm thick aluminum provides radiation shielding and so is unlikely the source of fluorescence.

8 Conclusion

This study of the populations of CRs and snowballs detected with NIRISS demonstrates that this instrument is highly sensitive to space weather at L2. The flux of particles striking its near-IR detector follows closely the solar cycle activity on a wide range of timescales. As the Sun enters the peak of Solar Cycle 25 in early 2024, it will generate impactful space weather events for several months and into 2025. The collection of deep NIRISS darks will continue in future JWST cycles so it will be possible to verify the trends observed so far in Cycles 1 and 2 throughout the solar maximum and into the following period of declining activity. Since the reference files of the calibration pipeline will be updated at 3-month intervals, it will be possible to capture the dependence of the detector properties (dark current, bias level, sensitivity, backgrounds, etc…) on the progression of the solar cycle.

9 References

Aldridge, D. et al. 2007, JWST FGS TFI Detector Assembly Design Document, JWST-RPT-009763

Blasi, P. 2013, The Origin of Galactic Cosmic Rays, Astronomy and Astrophysics Review, 21, 70

Bourque, M. & Baggett, S. 2016, WFC3/UVIS Dark Calibration: Monitoring Results and Improvements to Dark Reference Files, ISR WFC3 2016-08 (Baltimore: STScI)

Bushouse, H., Eisenhamer, J., Dencheva, N., Davies, J., Greenfield, P., Morrison, J., Hodge, P., Simon, B., Grumm, D., Droettboom, M., Slavich, E., Sosey, M., Pauly, T., Miller, T., Jedrzejewski, R., Hack, W., Davis, D., Crawford, S., Law, D., Gordon, K., Regan, M., Cara, M., MacDonald, K., Bradley, L., Shanahan, C., Jamieson, W., Teodoro, M., Williams, T., & Pena-Guerrero, M. (2024). JWST Calibration Pipeline (1.13.4). Zenodo. https://doi.org/10.5281/zenodo.10569856

Cillis, A. et al. 2018, Snowballs in Euclid and WFIRST Detectors, in Space Telescopes and Instrumentation 2018: Optical, Infrared, and Millimeter Wave, Proc. of SPIE Vol. 10698

Cooper, R. et al. 2023, NIRISS Commissioning Results: NIS-006 Darks (NGAS CAR-345, APT 1081), JWST-STScI-008397 (Baltimore: STScI)

Doyon, R. et al. 2023, The Near Infrared Imager and Slitless Spectrograph for the James Webb Space Telescope, I. Instrument Overview and In-flight Performance, PASP, 135:098001

Evans, S.W. et al. 2003, Natural Environment near the Sun/Earth-Moon L2 Libration Point, Marshall Space Flight Center (MSFC), Alabama

Evans, C. 2005, JWST FGS Preliminary Design Review Coating Designs, FGS PDR, JWST-PRES-006058

Evans Jensen, A. et al. 2013, Properties of Cathodoluminescence for Cryogenic Applications of SiO_2-based Space Observatory Optics and Coatings, in Cryogenic Optical Systems and Instruments, Proc. of SPIE Vol. 8863

Fu, S. et al. 2021, Variations of the Galactic Cosmic Rays in the Recent Solar Cycles, ApJS, 254, 37

Green, J., & Olszewski, H. 2020, IR Snowball Occurrences in WFC3/IR: 2009 – 2019, HST ISR 2020-03 (Baltimore: STScI)

Kress, B.T., Rodriguez, J.V., Boudouridis, A. et al. 2021, Observations from NOAA's Newest Solar Proton Sensor, Space Weather, 19, https://doi.org/10.1029/2021SW002750

Martel, A.R. 2020, Analysis of the NIRISS Detector Void in the CV3 and OTIS Cryo Campaigns, JWST-STScI-007123 (Baltimore: STScI)

Martel, A.R. and the NIRISS Team 2022, A NIRISS Commissioning Results: NIS-024 NIRISS FPA Heater On (NGAS CAR-757), JWST-STScI-008167 (Baltimore: STScI)

Martel, A.R. and the NIRISS Team 2023, A Summary of the Commissioning of JWST NIRISS, JWST-STScI-008232 (Baltimore: STScI)

Martel, A.R., Volk, K., & Cooper, R. 2023, NIRISS Cycle 1 Calibration Results: Overview of the Full-Frame Darks (PID 1497, CAL-NIS-001), JWST-STScI-008530 (Baltimore: STScI)

McComas, D.J., Bame, S.J., Barker, P., et al. 1998, Solar Wind Electron Proton Alpha Monitor (SWEPAM), Space Science Reviews, 86, 563

McCullough, P. 2009, Radioactivity in HgCdTe Devices: Potential Source of Snowballs, HST ISR 2009-44 (Baltimore: STScI)

Pickel, J.C. et al. 2004, Radiation Induced Transient Effects in HgCdTe IR Focal Plane Arrays, in Optical, Infrared, and Millimeter Space Telescopes, Proc. of SPIE Vol. 5487

Potgieter, M. 2013, Solar Modulation of Cosmic Rays, Living Rev. Sol. Phys., 10, 3

Rauscher, B.J. 2015, Teledyne H1RG, H2RG, and H4RG Noise Generator, PASP, 127, 1144

Regan, M. 2024, Detection and Flagging of Showers and Snowballs in JWST, JWST-STScI-008545 (Baltimore: STScI)

Rey, S.J. & Anselin, L. 2007, PySAL: A Python Library of Spatial Analytical Methods, Review of Regional Studies, Vol. 37, pp. 5-27

Rigby, J. et al. 2023, The Science Performance of JWST as Characterized in Commissioning, PASP, 135:048001

Rowlands et al. 2008, JWST FGS Focal Plane Assembly Requirements Specification, JWST-SPEC-009960

SILSO, World Data Center, - Sunspot Number and Long-term Solar Observations, Royal Observatory of Belgium, Brussels, on-line Sunspot Number catalogue: http://www.sidc.be/SILSO/, 2022 – 2024

Stone, E.C., Frandsen, A.M., Mewaldt, R.A. et al. 1998a, The Advanced Composition Explorer, Space Science Reviews, 86, 1

Stone, E.C., Cohen, C.M.S., Cook, W.R., et al. 1998b, The Solar Isotope Spectrometer for the Advanced Composition Explorer, Space Science Reviews, 86, 357

Volk, K. 2014, NIRISS/FGS Detector Selection: Snowball Analysis, JWST-STScI-003929 (Baltimore: STScI)

Waczynski, A. et al. 2005, Radiation Induced Luminescence of the CdZnTe Substrate in HgCdTe Detectors for WFC3, in Focal Plane Arrays for Space Telescopes II, Proc. of SPIE Vol. 5902

Acknowledgments

We thank the ACE SIS instrument team and the ACE Science Center for providing the ACE data.

Appendix A. Journal of the Dark Exposures of PIDs 1497 and 4473

The dark exposures of PIDs 1497 and 4473 are tabulated in Table A-1. The observation number, date, and time of the start of the exposures are given in the first, second, and third columns. Since the darks were inserted as pure parallels when the opportunity arose within the range of dates specified in the Special Requirements of the Dark template of the Astronomer's Proposal Tool (APT), we list the visit of the prime instrument in the fourth column as reported in the weekly release of the OP package and/or in the online JWST Weekly Observing Schedules. In the last columns, the RA and DEC of the telescope's +V1 axis (FITS header keywords RA_V1 and DEC_V1) in the ICRS coordinate system are tabulated.

Table A-1. Journal of PID 1497 and PID 4473 Dark Exposures

Observation	Date (UTC)	Time (UTC)	Prime Visit	RA (h m s)	Dec (° ′ ″)
1497:5	2022-08-08	02:40:49.691	1355:17:1	04 17 50.74	-47 46 18.13
1497:6	2022-08-13	00:08:41.190	1216:8:1	03 31 44.69	-27 58 12.92
1497:7	2022-08-26	18:54:12.560	1216:3:1	03 31 52.00	-27 49 29.53
1497:9	2022-09-11	20:39:10.859	1671:1:1	03 32 03.51	-27 51 19.37
1497:11	2022-09-14	21:59:24.034	2559:1:1	00 21 34.28	-71 56 01.72
1497:13	2022-10-12	23:44:32.509	1864:3:1	03 45 40.80	-52 02 11.94
1497:14	2022-10-13	04:35:15.052	1864:4:1	03 45 35.24	-52 02 02.67
1497:15	2022-10-27	05:28:39.172	2457:2:1	08 31 21.58	+16 12 10.99
1497:16	2022-10-27	23:03:46.054	1827:2:1	22 17 33.57	+00 28 32.84
1497:17	2022-11-11	07:37:33.942	2302:126:1	10 47 40.64	+55 07 00.74

Observation	Date (UTC)	Time (UTC)	Prime Visit	RA (h m s)	Dec (° ′ ″)
1497:18	2022-11-13	23:01:09.300	2457:3:1	08 34 10.68	+01 57 10.56
1497:19	2022-11-21	23:03:57.544	2654:5:1	07 49 05.88	+23 04 19.66
1497:20	2022-11-22	03:40:44.564	1893:1:1	22 28 40.92	-35 02 16.61
1497:21	2022-12-20	16:18:02.749	2754:1:1	00 38 25.45	-33 47 28.28
1497:22	2023-01-01	04:14:20.659	1198:12:1	04 38 21.92	-12 07 42.35
1497:24	2023-01-02	21:23:32.038	2391:8:1	10 11 00.65	-04 32 24.74
1497:41	2023-02-13	09:34:18.296	1208:62:1	04 16 38.55	-23 58 32.49
1497:27	2023-02-14	10:10:56.786	1967:9:1	15 12 01.45	+44 17 31.50
1497:28	2023-02-19	16:46:58.273	1706:4:1	08 25 40.39	-50 50 56.14
1497:29	2023-03-02	07:58:16.612	2473:66:1	14 45 34.96	-23 12 43.46
1497:30	2023-03-03	12:45:54.214	1706:1:1	08 26 46.81	-51 01 48.40
1497:42	2023-04-05	15:55:16.543	2555:1:1	15 47 01.82	-78 08 33.94
1497:33	2023-04-16	13:18:03.096	1186:1:1	18 29 18.00	+01 10 38.36
1497:34	2023-04-17	16:06:49.658	1230:7:1	08 55 38.97	-07 10 15.60
1497:37	2023-05-09	05:29:05.963	1217:9:1	10 01 01.92	+02 22 21.75
1497:38	2023-05-13	16:49:54.133	2331:4:1	19 36 29.67	+07 40 16.51
1497:31	2023-05-13	21:33:36.517	2331:16:1	19 36 27.79	+07 39 12.40
1497:32	2023-05-15	17:59:59.321	2331:21:1	19 36 27.35	+07 39 03.37
1497:39	2023-05-23	04:28:31.413	4426:1:1	12 37 46.63	+62 12 24.25
1497:1	2023-06-16	19:05:37.329	2567:29:1	12 34 46.41	+12 45 06.52
1497:2	2023-06-20	13:57:45.233	2567:38:1	12 32 54.20	+12 03 23.12
1497:3	2023-06-22	16:23:45.372	1967:7:1	11 47 37.16	-00 04 00.40
1497:4	2023-06-25	20:32:10.292	2567:35:1	12 31 12.89	+12 30 59.54
1497:40	2023-07-02	09:12:37.209	2177:3:1	13 33 40.49	+16 39 11.89
4473:1	2023-07-14	23:49:25.721	1964:2:1	15 31 29.31	+10 49 50.10
4473:3	2023-07-23	13:05:07.336	1970:2:1	01 21 19.12	+13 13 09.73
4473:5	2023-08-12	03:08:34.467	4554:2:1	16 32 19.27	+26 24 03.28
4473:6	2023-08-16	09:39:49.459	2905:1:1	17 36 22.25	+04 52 05.78
4473:7	2023-08-26	13:34:48.345	1908:3:1	04 15 37.47	-24 09 34.61
4473:11	2023-10-02	02:08:45.392	3743:1:1	02 01 51.76	-61 15 47.75
4473:12	2023-10-03	23:01:07.874	3743:4:1	03 44 13.45	-47 25 29.24
4473:2	2023-10-04	19:51:07.017	3743:10:1	21 33 06.38	-57 53 34.60

Observation	Date (UTC)	Time (UTC)	Prime Visit	RA (h m s)	Dec (° ′ ″)
4473:8	2023-10-13	19:09:50.300	2957:2:1	03 31 43.31	-27 45 41.81
4473:13	2023-10-30	03:29:36.021	4557:25:1	17 40 31.00	+69 09 32.59
4473:15	2023-11-09	18:40:06.879	3055:1:1	03 36 23.25	-34 49 48.63
4473:16	2023-11-10	22:36:54.553	1538:33:1	07 59 35.46	-10 49 18.61
4473:10	2023-11-11	10:56:49.966	2177:2:1	03 32 24.33	-27 40 27.66
4473:17	2023-11-28	12:58:22.996	1967:4:1	09 10 36.17	+01 50 26.72
4473:18	2023-12-09	11:15:11.458	2122:3:1	03 20 21.13	-19 23 42.94
4473:21	2024-01-03	17:54:15.361	2701:1:1	10 00 04.38	+02 06 09.91
4473:22	2024-01-10	20:27:31.774	4490:1:1	17 25 16.64	+60 34 57.88
4473:23	2024-01-29	11:29:51.586	3843:4:1	11 09 57.13	+64 50 28.91
4473:24	2024-02-06	19:14:40.664	4497:9:1	11 00 43.33	+71 28 31.61
4473:25	2024-02-11	02:10:26.506	4246:21:1	06 47 35.39	+70 04 49.74
4473:27	2024-02-25	14:02:20.223	3050:25:1	04 38 18.86	+26 52 21.95
4473:29	2024-03-15	17:31:31.116	3414:1:1	05 46 42.51	-00 07 44.77
4473:30	2024-03-20	17:53:39.193	3514:1:1	07 52 26.87	-76 26 19.87
4473:20	2024-04-29	07:17:54.887	4265:1:1	10 01 32.14	+02 36 57.02
4473:33	2024-05-07	00:40:28.075	3843:5:1	11 11 50.55	+64 58 24.04
4473:31	2024-05-10	16:45:39.669	3433:2:1	09 41 31.46	+07 46 46.40
4473:35	2024-05-11	17:19:40.799	4043:1:1	07 24 51.98	-73 31 43.55
4473:36	2024-05-14	19:26:31.507	3722:3:1	11 27 13.07	+42 18 27.78
4473:37	2024-05-27	22:28:38.735	2969:1:1	07 25 30.94	-73 30 25.19
4473:38	2024-05-29	06:26:58.515	2959:1:1	07 25 36.26	-73 29 51.09
4473:26	2024-06-03	16:18:59.438	3433:8:1	14 01 05.86	+62 27 00.54
4473:32	2024-06-05	13:38:46.723	3079:2:1	10 35 26.16	-14 23 56.47
4473:34	2024-06-05	18:57:44.560	4339:1:1	16 32 26.23	+24 30 06.27
4473:39	2024-06-20	20:06:59.026	4125:22:1	21 10 59.72	-01 22 54.95
4473:40	2024-06-24	22:17:54.197	4125:18:1	21 34 53.20	-01 10 07.34